Variability of the Atlantic Ocean North Equatorial Counter Current from 15 years of ADCP Observations and GLORYS12V1 Reanalysis

Djoirka Minto Dimoune[1], Fabrice Hernandez[2], and Moacyr Araujo[3]

[1]Universidade Federal do Pernambuco
[2]IRD
[3]UFPE

November 24, 2022

Abstract

Ocean current observations from different seasons of 15 years of vessel-mounted Doppler Current Profiler, merely from the PIRATA program, and drifters-derived near-surface currents are used to describe the structure, the variability of the North Equatorial Countercurrent (NECC) at 38{degree sign}W in the tropical Atlantic. Then used to validate the GLORYS12V1 ocean reanalysis, showing that the inferred NECC's characteristics present reliable realism. This allows further analysis of the NECC's seasonal and interannual variabilities over the full reanalysis period (1993-2018). The NECC presents an annual cycle of northward migration driven by the wind field with a two-cores structure. It exhibits a single branch, the sNECC, from December to June. With the addition of a second branch, the nNECC, the rest of the year. The sNECC starts the seasonal cycle in June, then grows northward, driven by the northward migration of the ITCZ with a three-month time lag. The nNECC core appears in August, migrates northward, then vanishes in December/January around 12{degree sign}N. From January to May the sNECC decays, with northward displacement toward 7-9{degree sign}N, driven by the second zero of the wind stress curl. From year to year, the NECC shows significant variations in relation with the tropical Atlantic zonal and meridional climate modes. First, positive NECC transport anomalies appear with "warm" meridional mode and zonal mode "Atlantic Niña" phases. Second, positive anomalies appear with weak meridional "cold" phase, and "Atlantic Niño" increasing zonal mode. Third, negative NECC anomalies occur with "cold" meridional phase and a negative zonal mode.

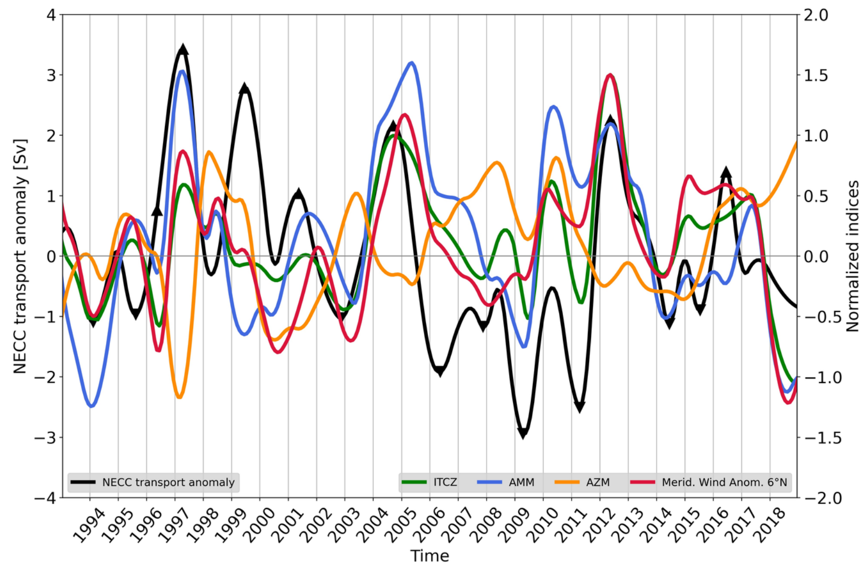
NECC transport anomaly [Sv]
Normalized indices
NECC transport anomaly
ITCZ
AMM
AZM
Merid. Wind Anom. 6°N
1994
1995
1996
1997
1998
1999
2000
2001
2002
2003
2004
2005
2006
2007
2008
2009
2010
2011
2012
2013
2014
2015
2016
2017
2018
Time

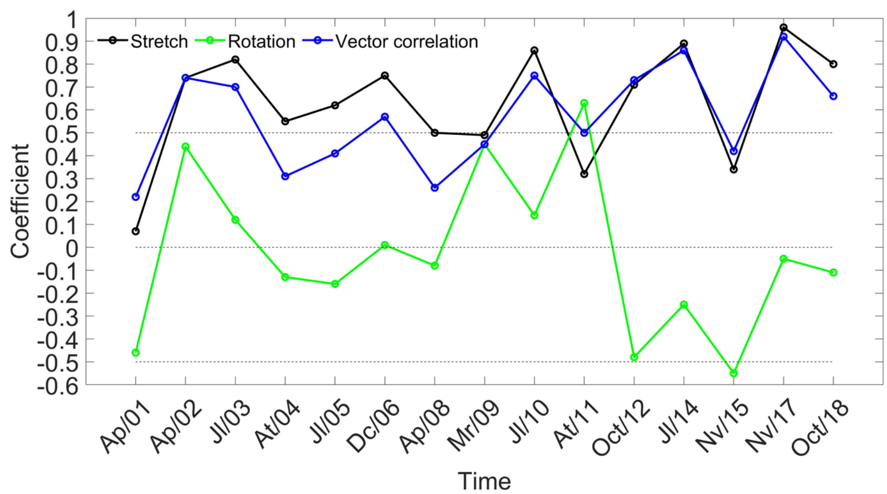
Stretch
Rotation
Vector correlation
Coefficient
Ap/01
Ap/02
Jl/03
At/04
Jl/05
Dc/06
Ap/08
Mr/09
Jl/10
At/11
Oct/12
Jl/14
Nv/15
Nv/17
Oct/18
Time

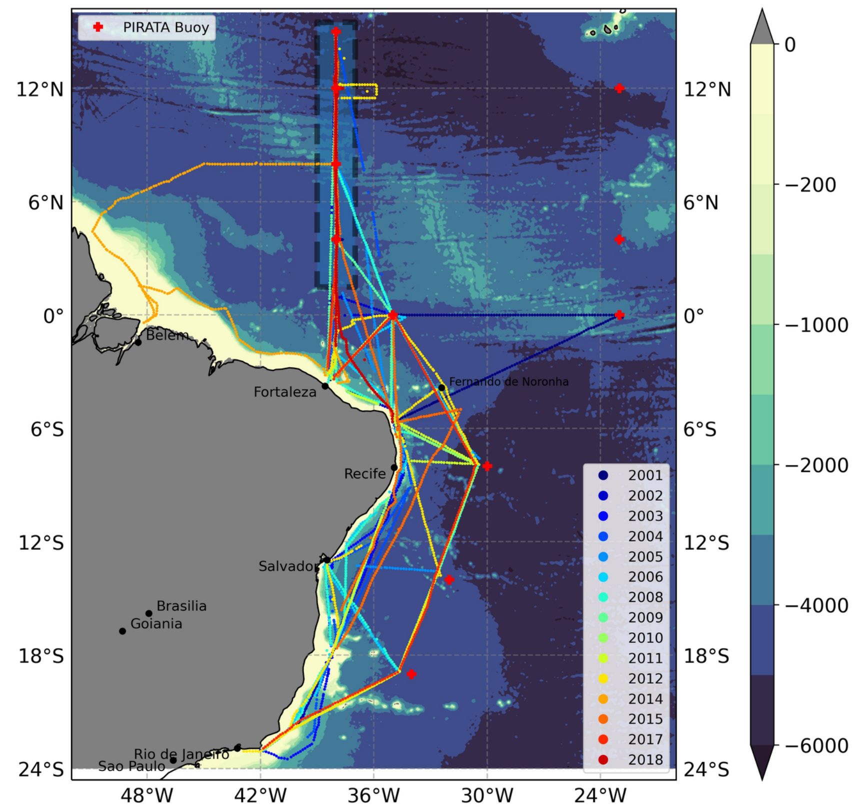
PIRATA Buoy
12°N
6°N
0°
6°S
12°S
18°S
24°S
48°W
42°W
36°W
30°W
24°W
Belem
Fortaleza
Fernando de Noronha
Recife
Salvador
Brasilia
Goiania
Rio de Janeiro
Sao Paulo
2001
2002
2003
2004
2005
2006
2008
2009
2010
2011
2012
2014
2015
2017
2018
0
−200
−1000
−2000
−4000
−6000

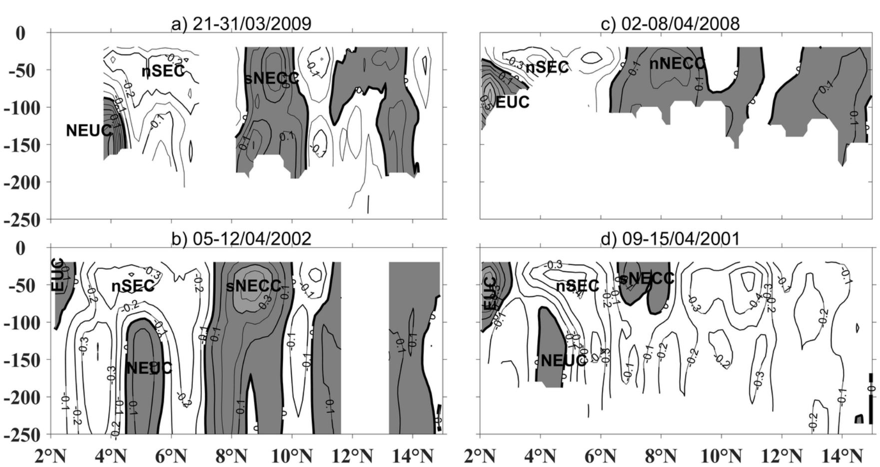
a) 21-31/03/2009
c) 02-08/04/2008
b) 05-12/04/2002
d) 09-15/04/2001
NEUC
nSEC
sNECC
EUC
nNECC
0
-50
-100
-150
-200
-250
2°N
4°N
6°N
8°N
10°N
12°N
14°N

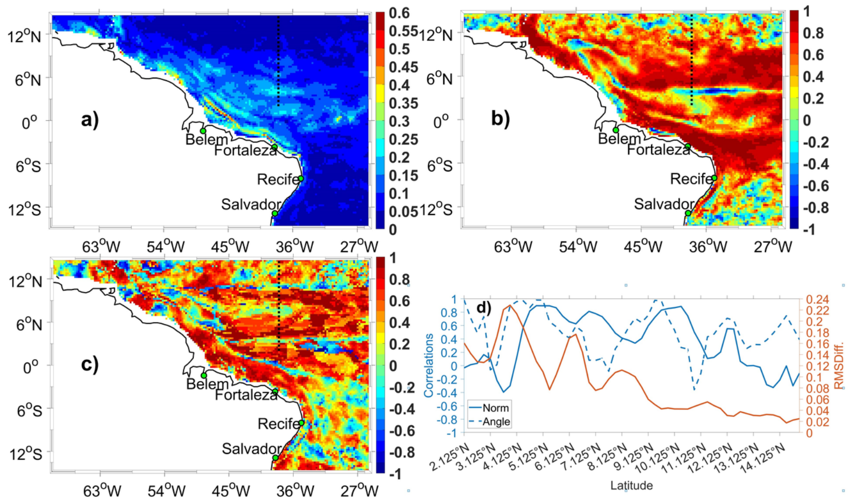
a)
b)
c)
d)
Belem
Fortaleza
Recife
Salvador
12°N
6°N
0°
6°S
12°S
63°W
54°W
45°W
36°W
27°W
Correlations
RMSDiff.
Latitude
Norm
Angle
2.125°N
3.125°N
4.125°N
5.125°N
6.125°N
7.125°N
8.125°N
9.125°N
10.125°N
11.125°N
12.125°N
13.125°N
14.125°N

Variability of the Atlantic Ocean North Equatorial Counter Current from 15 years of ADCP Observations and GLORYS12V1 Reanalysis

Djoirka M. Dimoune[1], Fabrice Hernandez[1,2], and Moacyr Araujo[1,3]

[1]Laboratorio de Oceanografia Fısica Estuarina e Costeira (LOFEC), Departamento de Oceanografia da Universidade Federal de Pernambuco (UFPE), Cidade Universitaria, Avenida Arquitetura s/n, 50740-550 Recife, PE, Brazil..

[2]Institut de Recherche pour le Développement (IRD), LEGOS, 18 avenue Edouard Belin, 31400 Toulouse, France.

[3]Brazilian Research Network on Global Climate Change (Rede CLIMA), Av. dos Astronautas, 1758, 01227-010 São José dos Campos, SP, Brazil.

Corresponding author: Dimoune Djoirka Minto (pmintodimoune@gmail.com)

Key Points:

- 15 years of currents from PIRATA and Brazilian campaigns in the Tropical Atlantic used to describe the North Equatorial Counter Current.
- The GLORYS12V1 global ocean reanalysis is proved to be reliable to study the North Equatorial Counter Current variability.
- The North Equatorial Counter Current seasonal cycle evolves with 2 branches, influenced over years by the Zonal and Meridional Atlantic Modes.

Abstract

Ocean current observations from different seasons of 15 years of vessel-mounted Doppler Current Profiler, merely from the PIRATA program, and drifters-derived near-surface currents are used to describe the structure, the variability of the North Equatorial Countercurrent (NECC) at 38°W in the tropical Atlantic. Then used to validate the GLORYS12V1 ocean reanalysis, showing that the inferred NECC's characteristics present reliable realism. This allows further analysis of the NECC's seasonal and interannual variabilities over the full reanalysis period (1993-2018). The NECC presents an annual cycle of northward migration driven by the wind field with a two-cores structure. It exhibits a single branch, the sNECC, from December to June. With the addition of a second branch, the nNECC, the rest of the year. The sNECC starts the seasonal cycle in June, then grows northward, driven by the northward migration of the ITCZ with a three-month time lag. The nNECC core appears in August, migrates northward, then vanishes in December/January around 12°N. From January to May the sNECC decays, with northward displacement toward 7-9°N, driven by the second zero of the wind stress curl. From year to year, the NECC shows significant variations in relation with the tropical Atlantic zonal and meridional climate modes. First, positive NECC transport anomalies appear with "warm" meridional mode and zonal mode "Atlantic Niña" phases. Second, positive anomalies appear with weak meridional "cold" phase, and "Atlantic Niño" increasing zonal mode. Third, negative NECC anomalies occur with "cold" meridional phase and a negative zonal mode.

Keywords:

Tropical Atlantic, Western boundary, NECC, ITCZ, Atlantic climate modes, Observations, Ocean Reanalysis

Plain Language Summary

The North Equatorial Countercurrent (NECC) lays around 4°-10°N across the Tropical Atlantic, transporting eastward warm and anomalous salt waters, forced essentially by the Trade Winds. It can be observed during oceanographic cruises, like PIRATA at 38°W. Its variations since 1993 can be studied with the GLORYS12V1 reanalysis, numerical simulation representing the ocean circulation. The realism of GLORYS12V1 currents is evidenced by comparison to observations. The NECC seasonal cycle is directly influenced by the North-East and South-East Trade Winds pattern over seasons. The sNECC branch starts the cycle in June around 5°N and grows. Then the nNECC branch appears in August with a core at its northern flank, that migrates northward, eventually vanishes after December around 12°N. From January to May the sNECC moves and decays toward 7-9°N. The NECC also changes over years, in relation with the "meridional" and "zonal modes" climatic pattern affecting the Tropical Atlantic, with large regional temperature anomalies. Over 25 years, we found that three main scenarii link the NECC with these two modes. Two, with more intense NECC linked either with "warm" meridional mode and "cold" zonal mode, or with the opposite situation. Then a less intense NECC associated with "cold" zonal and meriodional modes.

1 Introduction

The Western Tropical North Atlantic Ocean (WTNA) witnesses a complex circulation resulting from direct interactions with the atmosphere, and interhemispheric water mass exchanges over the entire Atlantic basin linked to the global circulation (Bourlès et al., 1999; Stramma and Schott, 1999; Urbano et al., 2008). The western boundary circulation, like other basins wind-driven circulation, is feed by the north and south subtropical gyre waters through the zonal westward North and South Equatorial Currents (NEC and SEC). Interhemispheric heat and water mass exchanges are mostly linked to the global thermohaline circulation through the so-called Atlantic Meridional Overturning Circulation (AMOC). Part of the water masses from both hemisphere reaching this western boundary region are redistributed eastward in the tropical band (Philander and Pacanowski, 1986). Redistribution occurs at depth and above the thermocline with the Equatorial Undercurrent (EUC), then in the 3-6° latitude bands with the North and South Equatorial Undercurrent (NEUC, SEUC). At the surface, warm and rich-oxygen waters are transported into the northern tropics by the North Equatorial Countercurrent (NECC), as shown by Figure 1 of Schouten et al. (2005) or Castellanos et al. (2015). The NECC path is associated with a zonal band of Sea Surface Salinity (SSS) variability (Figure 1), due in particular to the transport of Amazon River Plume fresher water from spring to fall toward the central Tropical Atlantic (Coles et al., 2013; Varona et al., 2019). The NECC is partly fed by the retroflection of the North Brazilian Current (NBC), which occurs around 6.6±2°N, clearly exhibited by first paths of surface drifters in the region (Richardson and Reverdin, 1987), and by waters from the NEC (Bourlès et al., 1999; Fonseca et al., 2004; Schott et al., 1998; Wilson et al., 2002). Extending from 2-15°N in the west, the NECC mean signature narrows between 2-10°N at 25°W, then extends towards the Gulf of Guinea (Figure 1), feeding along its northern coast the Guinea Current (Lumpkin and Garzoli, 2005). From 44°W to 22°W the NECC dynamics has been shown to be in balance between the local Ekman pumping and the geostrophic current divergence, and the wind stress curl (Garzoli and Katz, 1983).

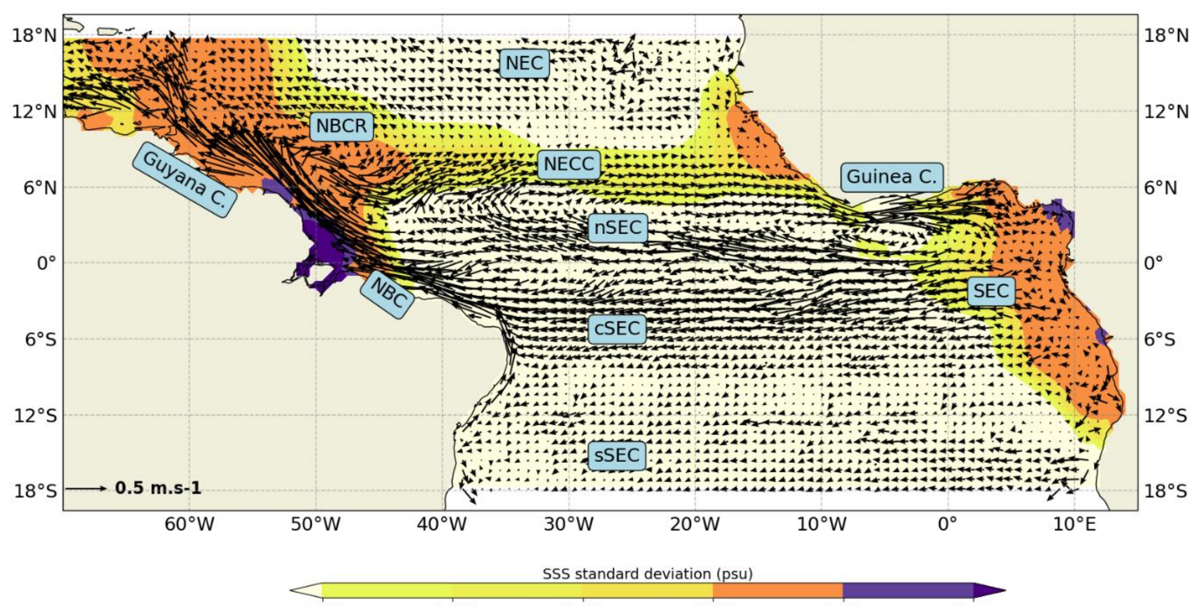

Figure 1. Surface currents from the AOML annual drifter-derived climatology in the tropical Atlantic (units m/s). Superimposed the standard deviation of the SSS for the period January 1993 to December 2018 (units psu). Main currents discussed in the text are also highlighted.

The NECC spatial and temporal variability has been assessed with many approaches in the past. Ship-drift estimates, Inverted Echo Sounders (IES), conductivity-temperature-depth (CTD), surface drifters and satellite altimetry showed that the NECC flows within the band 10-50°W and 3°N and 10°N (Carton and Katz, 1990; Didden and Schott, 1992; Garzoli and Richardson, 1989; Garzoli, 1992; Katz, 1981; Richardson and McKee, 1984; Stramma, 1991; Stramma and Schott, 1999). Model approach, like Urbano et al. (2006) and Varona et al. (2019) showed that the NECC extends from 3 to 13°N at 35°W, and confirmed the presence of the NECC's two-cores pattern mentioned earlier by Didden and Schott (1992) with GEOSAT satellite altimetry. Which pattern is justified by the meridional broader shape of the InterTropical Convergence Zone (ITCZ) and the wind stress. The two-cores structure has been confirmed by Urbano et al. (2008) using near surface drifter-derived currents and 6 years of Acoustic Doppler Current Profiler (ADCP) and hydrographic data from PIRATA cruises (Bourlès et al., 2008; Bourlès et al., 2019). In July, the NECC northern core (nNECC) bifurcates and establishes northward in August-September, around 13-14°N. Fonseca et al. (2004) show that the NECC occupies two northernmost positions along the year. First between October and December, due to the ITCZ northward migration in late summer, followed by the northward shift of the NECC with a 2-3 months lag corresponding to time propagation of Rossby waves in this region. Then in February, forced by the secondary wind stress curl minimum associated with the wind stress divergence located near 12-15°N during Spring. The Figure 2 depicts the wind stress climatological pattern and this northern minimum in April when the NECC transport is low and when it is high in October. Urbano et al. (2008) also showed that, from boreal spring to summer, the subsurface NEUC located south of 5°N in the upper thermocline shifts northward, surfaces, and merges on the vertical to feed the NECC's southern core (sNECC) that strengthens during the boreal summer.

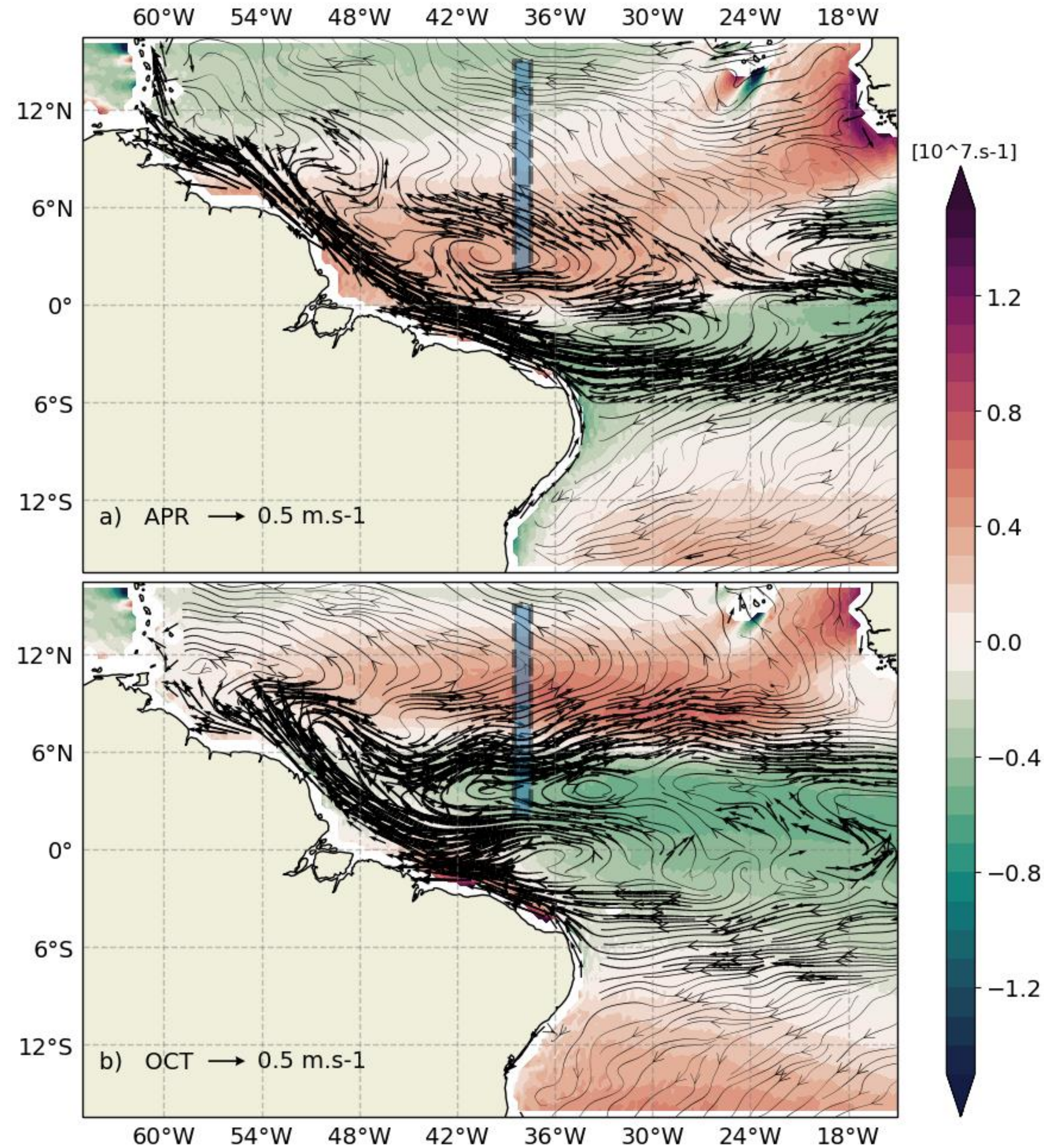

Figure 2. Monthly mean currents from the AOML drifter-derived climatology (m/s) in the western tropical Atlantic (15°S-15°N, 65-15°W°), superimposed on ERA5 wind curl monthly climatology (units: s-1) for respectively April (a) and October (b). The dashed line represents the ADCP section of interest at 38°W.

The NECC shows also a strong seasonal cycle, with a minimum flow in spring and the maximum during the summer (Fonseca et al., 2004; Urbano et al., 2006; Urbano et al., 2008), and variation of the mesoscale activity associated by the NECC and the NBC Retroflection (NBCR) (Castelão and Johns, 2011; Garzoli et al., 2004; Goni and Johns, 2001). Aguedjou et al. (2019) suggest barotropic instability mechanisms for this eddy generation.

The interannual variability of the NECC has been less discussed, certainly because the annual harmonic represent more than 80% of the large scale circulation variability in the WTNA (Richardson and Walsh, 1986). Based on satellite altimetry and hydrographic data from 1993 to 2000, Fonseca et al. (2004) show a year-to-year variation of the NECC. The link between wind, ITCZ position and NECC strength and location has been further investigated by Hormann et al. (2012). Using satellite altimetry, wind and drifter velocities time series over several years. They show relation between the NECC interannual variability and the two dominant climate mode of the tropical Atlantic. A strengthening of the NECC, associated with a northward shift of the ITCZ seems predominant during the positive phase of the Atlantic Meridional Mode (AMM), when the northern hemisphere is warmer-than-normal. Then, the southern flank of the NECC lies into the equatorial band. They conclude that the Atlantic Zonal Mode (AZM) negative phase also contributes to the intensification of NECC, when the equatorial thermocline is deeper in the west due to Bjerknes Feedback mechanism.

Several studies are discussing so far the NECC dynamics and variability, using observations with relevant spatial coverage, but usually spanning over a rather short period. We revisit here this NECC description using 15 years of ADCP in the WTNA, obtained during the PIRATA Brazilian-ship cruises along the 38°W, and the CAMADAS FINAS sea campaign, complemented on the overall region using a drifter-derived near-surface currents climatology data, and the GLORYS12V1 global ocean reanalysis (herein after G12V1) over the 1993-2018 period. The in-situ dataset are first used to validate G12V1, further analysed to investigate the seasonal and the interannual variabilities of the NECC and their possible relations with the wind stress, and the Atlantic climate modes. This work is presented in five parts. First, the data (ADCP section, drifter climatology, G12V1 reanalysis and ERA-5 wind) are described. The zonal velocity features and the NECC total zonal transport in the upper layer at 38°W from ADCP measurements are examined next. The third part is devoted to the G12V1 reanalysis validation. From it, the fourth part presents the description of the seasonal variability of the NECC at 38°W, then of the interannual variability in relation to the Tropical Atlantic Variability. Finally, results are discussed before concluding. We remind that in this work, we use the boreal season definition referred to the northern hemisphere.

2 Data source and processing

2.1 ADCP data processing

Since 2001, several ship-mounted ADCP (SADCP) surveys have been performed on board Brazilian research vessels on the vicinity of the 38°W section (Figure 3). First, Brazilian cruises maintaining yearly the PIRATA moored buoy program. Until 2016, using the Research/Vessel R/V Antares, equipped with an Ocean Surveyor 75 KHz ADCP system. Then, the brand-new R/V Vital de Oliveira took over, equipped with a dual frequency-band Ocean Surveyor working at 75 KHz and a broad-band at 150 KHz. Second the ADCP profiles obtained during the Camada Finas III experiment, that occurred 9-31 October 2012, with the research vessel NHo. Cruzeiro do Sul - H38 (DHN/Brazilian Navy). This ship was equipped with a Teledyne RD Ocean Surveyor ADCP working at 75 KHz. All these SADCP use a Vessel-mounted Data Acquisition System software (VmDAS) to collect raw vertical profiles along the ship route. For this study, ADCP data from every cruise along the repeated section at 38°W from

2°N to 15°N are selected, even if the Camadas Finas III cruise only sampled this section from 2°N to 8°N. The Table 1 sum-up the different durations of sections considered, the seasons linked to all of them, and others information about the cruises.

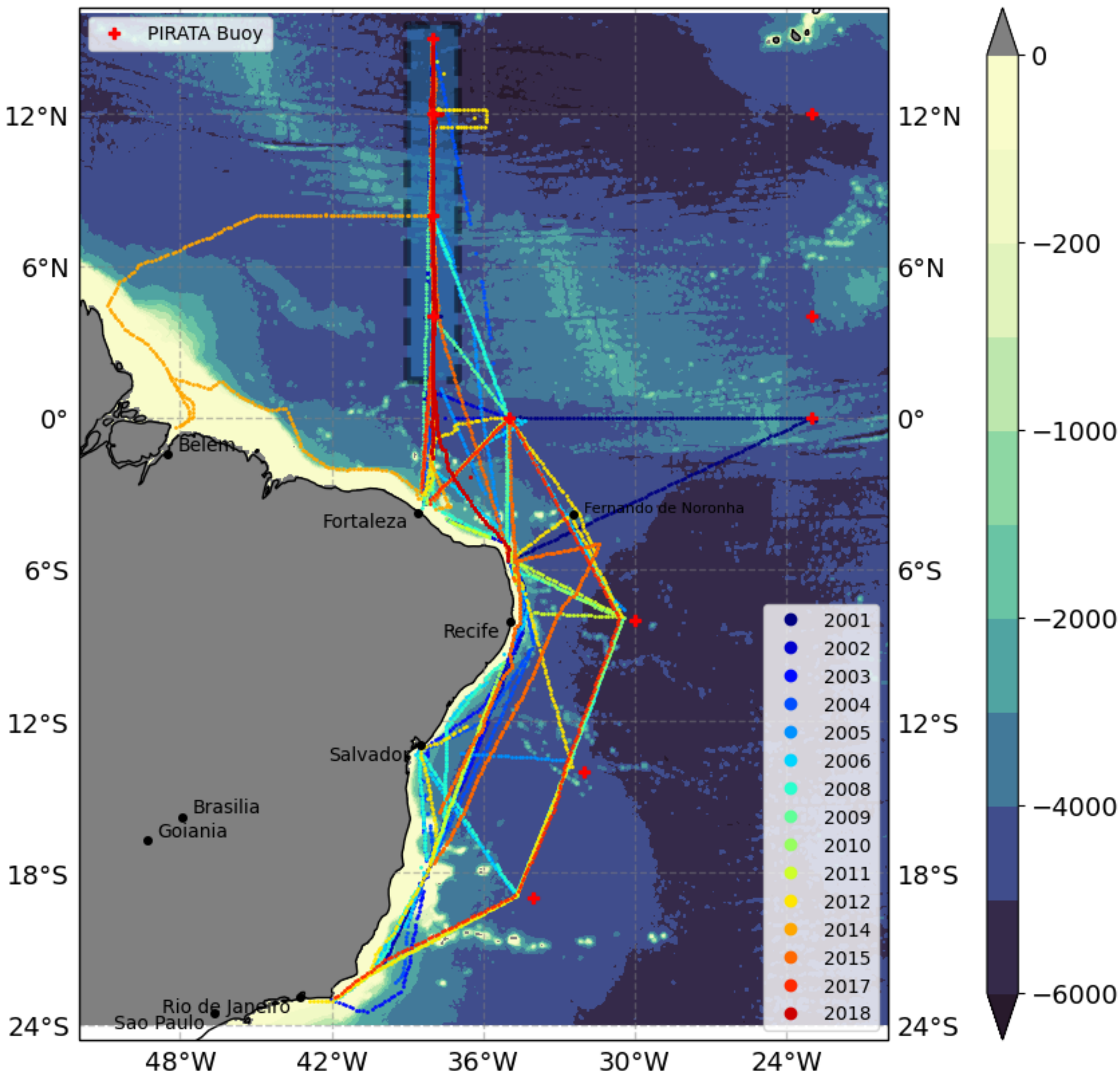

Figure 3. PIRATA-BR cruises since 2001 and Camadas Finas III (2012) vessel-mounted ADCP sections. A color code is attributed to identify cruise's routes each year. PIRATA moored location are indicated (red crosses). Underlying bathymetry from the ETOPO2 dataset is shaded. Black dashed rectangle define the area where ADCP data are considered in this work, along the 38°W section.

Table 1. *Names and Characteristics of PIRATA-BR and Camadas Finas cruises at the section 38°W: cruise, year, latitudinal coverage, duration of the section, and research vessel.*

Cruise	Year	Latitud. coverage	Duration of the section	Boreal season	Research Vessel
PIRATA BR XVII	2018	2°N-15°N	19-26 October	Fall	Vital de Oliveira
PIRATA BR XVI	2017	2°N-15°N	14-22 November	Fall	Vital de Oliveira
PIRATA BR XV	2015	2°N-15°N	27 October to 03 November	Fall	Antares
PIRATA BR XIV	2014	2°N-15°N	23-28 July	Summer	Antares
Camadas Finas	2012	2°N-8°N	27-31 October	Fall	Cruzeiro do Sul
PIRATA BR XIII	2011	2°N-15°N	23 August to 13 September	Summer	Antares
PIRATA BR XII	2010	2°N-15°N	24-30 July	Summer	Antares
PIRATA BR XI	2009	2°N-15°N	26-31 March	Winter	Antares
PIRATA BR X	2008	2°N-15°N	02-08 April	Spring	Antares
PIRATA BR IX	2006	2°N-15°N	01-07 December	Fall	Antares
PIRATA BR VIII	2005	2°N-15°N	14-19 July	Summer	Antares
PIRATA BR VII	2004	2°N-15°N	27-31 July	Summer	Antares
PIRATA VI	2003	2°N-15°N	17-31 July	Summer	Antares
PIRATA BR V	2002	2°N-15°N	05-12 April	Spring	Antares
PIRATA BR IV	2001	2°N-15°N	09-15 April	Spring	Antares

Under good sea-state conditions, the raw 75KHz SADCP data can provide reliable upper ocean velocity profiles down to 600-m-depth. It can be reduced to less than 100-m-depth in case of bad sea state conditions, associated most of the time to intensified trade winds, larger waves and surface currents. In this case, the ship stability along its route is reduced, as well as the acoustic signal penetration, unable to reach the deepest layers (Urbano et al., 2008). During the 2014 cruise, the maximum depth reached was less than 100 m. The acoustic downward ping is processed in 8-m length bin vertical resolution. Near the surface, velocity profiles are considered reliable from 16-m-depth downwards (Urbano et al., 2008). Along the ship route, the 2-minutes VmDAS raw data are processed using the version 7.2 of the validation and visualization software, CASCADE (Chaîne Automatisée de Suivi des Courantomètres Acoustiques Doppler Embarqués) developed at Ifremer Laboratoire de Physique de Océans (LPO, Brest, France) (Kermabon et al., 2018). Individual vertical profiles are first calibrated using the velocity between bin 3 and 5, considered as the more reliable. Then the ETOPO2 bathymetry along the ship route is used to discard bins contaminated by the seafloor interference. The absolute current along the vertical profile is computed using the Global Positioning System (GPS) and the standard shipboard gyroscopic compass heading and navigation values. Then, editing of erroneous estimates is performed using a threshold of the vertical speed to 100 cm/s ; the vertical shear to 0.2 s-1 ; the maximum current speed to 400 cm/s ; a discrepancy to averaged surrounding pings less than 3 standard deviation ; a signal to noise value larger than 60 over 170 ; and the profile is kept if more than 10% of the bins are not erroneous. Then, if needed, the misalignment and amplitude error detected at the first have been corrected. The TPOX9 barotropic tide model is applied to correct tidal errors, and edit outliers in the timeseries. Once validated, the 2-minutes vertical profiles are low-pass filtered over 20 minutes, at each depth. Finally, along the ship route, the vertical section is re-sampled every 15 km.

This dataset is a unique opportunity to characterize currents associated with the NECC along 38°W, between 2°N to 15°N, and provide valuable time variability of structures throughout the year.

2.2 GLORYS12V1 global ocean reanalysis

The G12V1 reanalysis provides a 3D description of the ocean circulation at the mesoscale in the WTNA. Global ocean numerical simulations offer a self-consistent representation of the circulation from the surface to the bottom, anywhere in the world ocean, and in a continuous timeline. The Mercator Océan G12V1 reanalysis covers the 1993-2018 period, with a 1/12° horizontal resolution. It is delivered through the Copernicus Marine Environment Monitoring Service (CMEMS, https://marine.copernicus.eu/) and described in the QUID_001_030 report (Drévillon et al., 2018), available at http://marine.copernicus.eu/documents/QUID/CMEMS-GLO-QUID-001-030.pdf. This reanalysis configuration is based on the 1/12° global operational system of Mercator Océan (Lellouche et al., 2018). It uses the NEMO3.1 ocean/sea-ice general circulation model (Madec, 2008), with the ORCA12 global configuration developed by the DRAKKAR consortium (The DRAKKAR Group et al., 2014) with 50 vertical levels. It is forced at the surface by the ECMWF ERA-Interim reanalysis, after some specific corrections. All along the simulation, data assimilation is performed using a reduced-order Kalman filter with a 3D multivariate modal decomposition of the background error, which includes an adaptive-error estimate and a localization algorithm. CMEMS along track altimeter data (Sea Level Anomaly – SLA), satellite Sea Surface Temperature (SST), and Sea Ice Concentration are assimilated. Together with in situ temperature and salinity (T/S) vertical profiles from the CORA database (Cabanes et al., 2013). Moreover, a 3D-VAR scheme provides a correction for the slowly-evolving large-scale biases in temperature and salinity. The simulation is initialized using the T/S conditions derived from the EN4.2.0 data base (Good et al., 2013).

In the present work, G12V1 (G12V1) daily horizontal velocity have been interpolated under the ADCP section at 38°W every 15 km. G12V1 monthly estimates over the WTNA are also downloaded for the seasonal and interannual analysis of the NECC, discussed later.

2.3 Other dataset

The drifter-derived climatology of near-surface current based on surface drifter trajectories from the Global Drifters Program (GDP) between 1979 and 2015 is used. Produced by the Atlantic Oceanographic and Meteorological Laboratory of the National Oceanic and Atmospheric Administration (AOML/NOAA, http://www.aoml.noaa.gov/phod/dac/index.php) (Laurindo et al., 2017). Using the 6 hours velocities, after slip correction, drogue loss evaluation, and 5-day low-pass filtering, the climatological monthly circulation has been mapped on a 0.25° resolution grid. The 12 months of this climatology are extracted into the WTNA (15°S-15°N and 25-70°W).

The ERA5 dataset provide surface wind information produced recently by the European Centre for Medium-Range Weather Forecasts (ECMWF, http://www.ecmwf.int) from January 1950 to Near Real time (NRT), and distributed by the Copernicus Climate Change Service (C3S). ERA5 combines large amount of information into global estimates using advanced modelling and a 4-dimensional variational analysis with a 12-hour analysis window (details at https://confluence.ecmwf.int/display/CKB/ERA5+data+documentation). 10 meters height monthly zonal and meridional components wind velocity fields of spatial resolution of 31km (0.28125 degrees) from 1993 to 2018 have been used in this work.

The National Oceanic and Atmospheric Administration (NOAA), produces a weekly Sea Surface Temperature (SST) global product on 0.25°grid, using the Optimum Interpolation (OI) analysis method: NOAA OI SST v2. This analysis uses in situ and bias corrected satellites SSTs. Technical details are given by Reynolds et al. (2002). From this weekly dataset, monthly global SST averages are also produced (available at https://www.esrl.noaa.gov/psd/data/gridded/data.noaa.oisst.v2.html). We considered this monthly dataset from 1993 to 2018 over the WTNA region.

From the CMEMS, the monthly SSS gridded are also downloaded over 1993-2018 in the WTNA (product name INSITU_GLO_TS_OA_REP_OBSERVATIONS_013_002_b). Produced by the ISAS objective mapping tool on a 0.5° grid (Gaillard et al., 2016) using in-situ temperature and salinity edited and corrected by the Coriolis data centre.

3 Zonal velocity fields from ADCP and NECC total zonal transport in the upper layer

Each ADCP section at 38°W is analyzed between 2-15°N in order to identify the different currents, their extension and intensity (Figures 4 and 5). The NECC branches are determined following three criteria. First the residual northern branch of the NECC (nNECC) is neglected during March and April, when its annual migration northward is ending, considering the annual cycle NECC's displacement proposed by (Urbano et al., 2008). Second, during the second half of the year, when the sNECC and nNECC are not yet separated and form a single core current, its latitudinal extension is defined by its two northern and southern edges by positive eastward velocities. Third, for each branch the central position of its core is given by the maximum velocity value. In 2004 and 2011, the ADCP surveys are rather limited (Figures 5j and 5e) and are plotted for later comparison with GLORY12V1. In October 2012 and July 2014 (Figures 5d and 5g) while limited, these surveys allow to define the NECC structures. All other surveys are used to compute zonal transport, applying interpolation to fill gaps along the section if needed.

Four main currents appear over these surveys at 38°W. The Equatorial Undercurrent (EUC) partly observed at the southern side. Part of the NEUC, the northern branch of the SEC (nSEC) and the NECC with its two branches during the second half of the year. The EUC appears during Spring (Figure 4) indicating a broader northward extension than in other seasons (Figure 5). In April 2008 (Figure 4c) it extends toward 4°N with a 0.6 m/s core at 2.5°N and 85m-depth. During this season, the EUC is constrained at its northern boundary by a strong westward nSEC (also visible in Figure 2a) that extends deeper than 100m-depth. The eastward NEUC, below 100m-depth and between 4-6°N is also visible during the Spring ADCP sections (Figure 4). There is no clear connection near the surface between the EUC and NEUC, despite what was suggested by Urbano et al. (2008). However, during the second half of the year, there is evidence of the connection between the NEUC and the NECC proposed by Rosell-Fieschi et al. (2015); Urbano et al. (2008). The nSEC is then strong (0.9m/s in July 2014 at 2.5°N and 35m-depth, Figure 5g), but more southward, maintaining the NEUC between 4-6°N. The NEUC and NECC connections are visible in 2003 -yet stated by Urbano et al. (2008), 2005, 2006, 2010, 2015, 2017 and 2018 (Figures 5k, 5i, 5f, 5h, 5c, 5b, 5a, respectively). This is in July 2010 that the NEUC appears deeper, with a maximum core velocity of 0.4 m/s between 3.5°N and 4.5°N at 180m-depth. At the opposite, in April 2001, the NEUC and the sNECC are both weak and well separated by the nSEC, strong and deeper (Figure 4d).

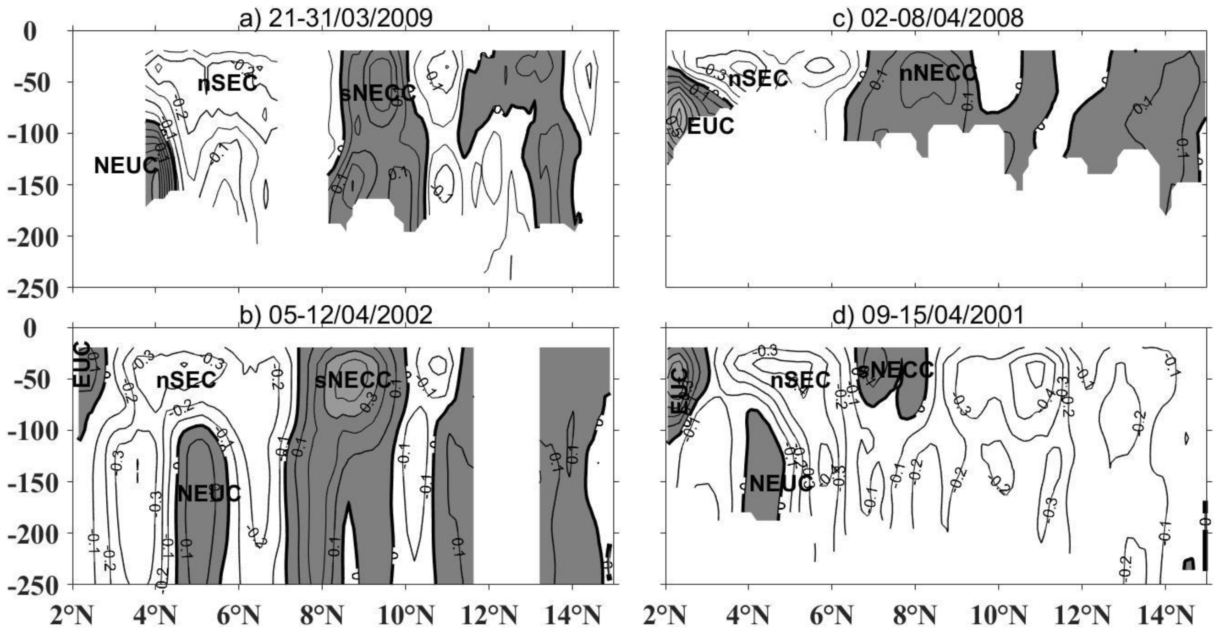

Figure 4. Zonal ADCP velocity (m/s) from 2°N to 15°N at section 38°W during Spring: a) March 2009, b) Apr 2002, c) Apr 2008, d) Apr 2001. Shaded gray and white areas represent respectively the eastward (positive) and the westward (negative) velocities with contours each 0.1 m/s. The zero-contour in black thick line.

The NECC is visible in every section, but with a pronounced seasonal pattern, weak during Spring and stronger during the second half of the year (Figure 5) during which it exhibits a second core, and later a second branch (Didden and Schott, 1992; Schott and Böning, 1991; Urbano et al., 2006; Urbano et al., 2008). The NECC lies between 2°N and 12°N, with the sNECC and nNECC flowing respectively between 3°N and 9.5°N, and 6.5°N and 12°N, separated by a westward flow, although in July 2003 and 2010 (Figures 5k and 5h) there is no separation yet. The sNECC highest maximum core velocity is observed in July 2003 (1.1 m/s at 6.5°N and 50m-depth). At the same depth, the nNECC highest maximum core velocity appears in July 2010 (Figure 5h) with 0.4m/s. From August to December (Figures 5a to 5f), due to the effect of the northward migration of ITCZ mentioned above, the NECC follows that migration, becoming larger with the two separated branches. The sNECC highest core velocities are noticed in October 2018 and November 2017 (Figures 5a and 5b) with values of 1.1m/s around 4.5- 5°N, both located at 60m-depth. The nNECC is weaker (maximum core velocity of 0.3 m/s observed at 9.5°N and 55m-depth in November 2015, Figure 5c).

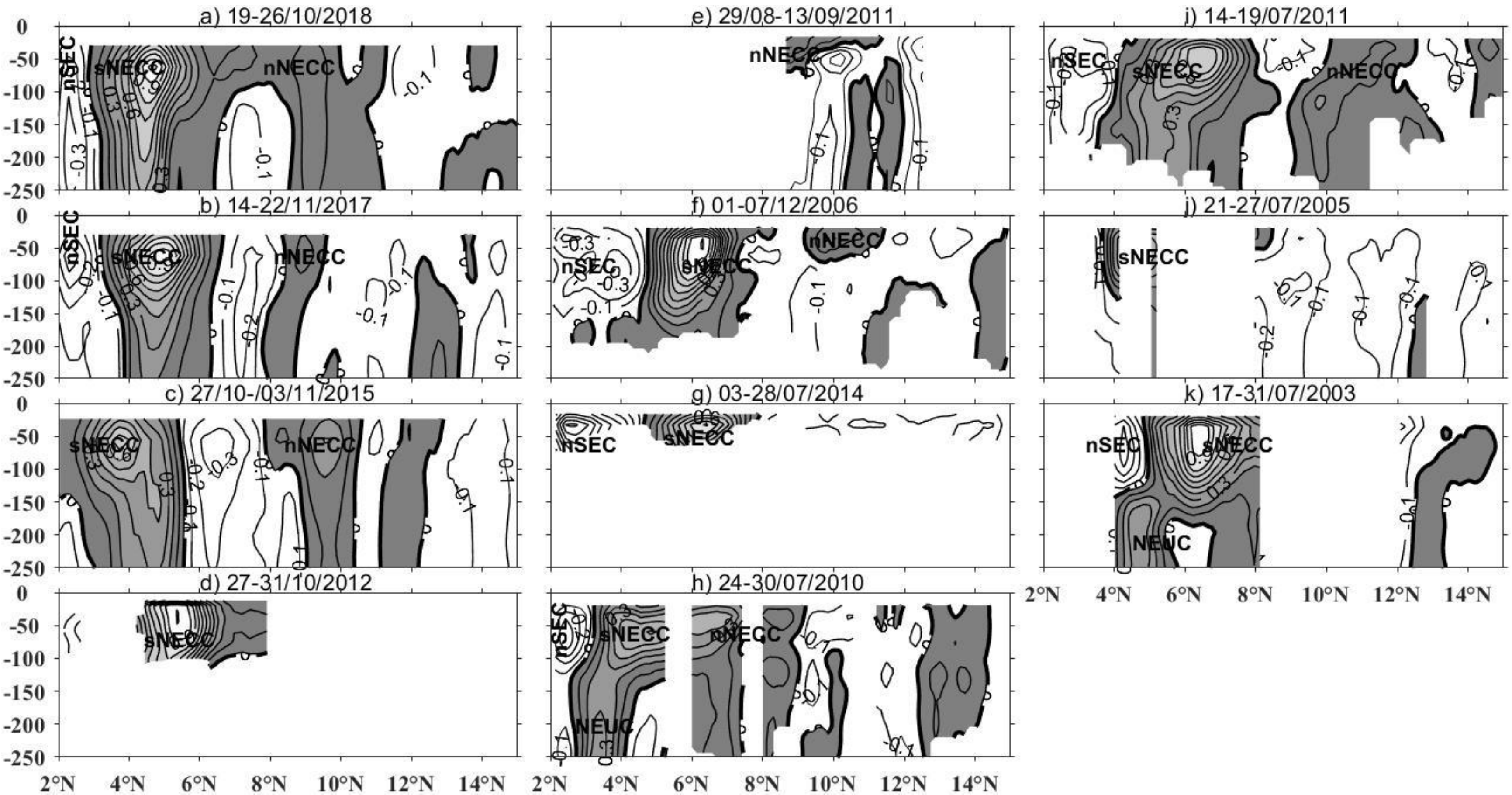

Figure 5. Same as Figure 4 for the second half of the year: a) Oct 2018, b) Nov 2017, c) Oct/Nov 2015, d) Oct 2012, e) Aug/Sep 2011, f) Dec 2006; and for July: g), h), i), j), k) July 2014, 2010, 2005, 2004 and 2003.

This northward migration and the NECC two branches vanish during the Spring of the next year. In march 2009 (Figure 4a), the sNECC core (0.3m/s) is at 8°N and 45m-depth with a value of 0.3 m/s. In April 2008 (Figure 4c), it flows between 6-9.5°N, with a core of 0.3m/s located around 8°N and 35m-depth. The nNECC becomes weaker, but a remnant flow can keep active at 12°N and merge with the next year brand new nNECC in October-December (Urbano et al., 2008). At the northernmost position of the 38°W ADCP profiles, during Spring, the southern edge of the NEC can be visible, in particular if the sNECC and nNECC are weak. This is the case in April 2001 (Figure 4d).

Once the NECC westward flow has been located in every ADCP section, its transport is computed, despite the lack of measurements below 100-m-depth some years. Considering typical thermocline depth in the WTNA varying from 100 to 150m-depth according to the season (Urbano et al., 2006; Verdy and Jochum, 2005), the transport is computed by vertical integration from 30m-depth (reliable limit for the ADCP) to 100, 150 and 200-m-depth whenever possible. In agreement with the above description of the NECC's seasonal pattern, its transport also varies with season (Figure 6): minimum/maximum respectively the first and second part of the year. The maximum transport mean value of 22.8±4 Sv is obtained for the period of October/November/December between 30m and 200m (18.9±2.3 Sv, and 14.6±1.7 Sv respectively, between 30-150-m and 30-100m-depth). The minimum value is obtained in March/April for the same range of depth with respective values of 5.4±3.1 Sv, 4.4±2.1 Sv and 3.4±1.8 Sv. Over all the cruises (Figure 6a) the maximum NECC transport is obtained in November 2018: 28.9 Sv between 30-200m-depth, and the minimum in April 2001: 1 Sv for the same depth range. In practice, 60% of the total transport is located in the 30-100m-depth range.

These transport values are in the range of previous study estimations, indicating NECC transports from 7 to 22Sv, reduced at 23°W to 8.5 Sv. Among the 13 Sv estimation of southern waters crossing the equator and entering the northern subtropical gyre, 3-5 Sv may be transported by the seasonal northward shift of the NECC from boreal fall to next spring and between 2 and 8 Sv may transit into the NBC, recirculate zonally eastward in the NECC and exit northward east of 23W (Chepurin and Carton, 1997).

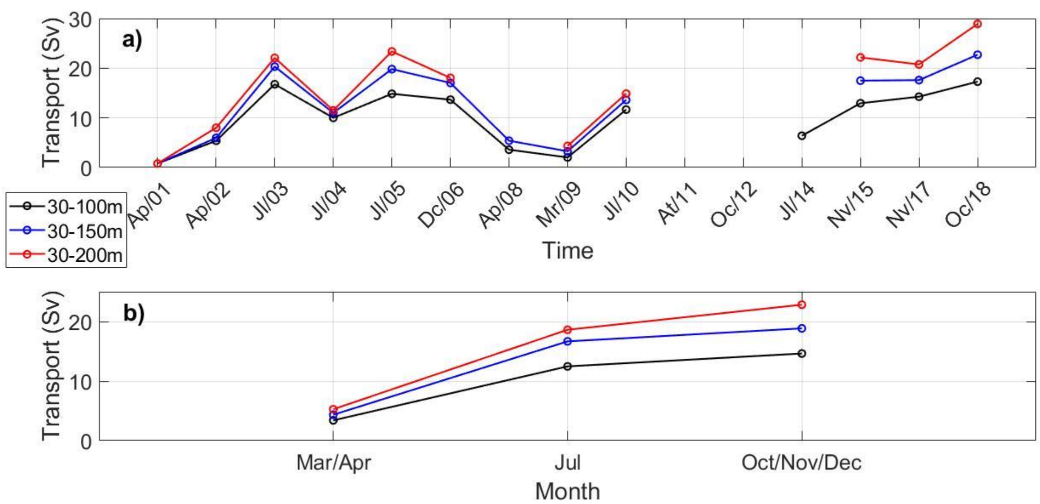

Figure 6. a) NECC total zonal transport (in Sverdrup) computed over every 38°W section between 30-100m-depth (black), 30-150m-depth (blue), and 30-200m-depth (red). b) same values averages per seasons.

4 Validation of GLORYS12V1 reanalysis and seasonal variability of the NECC at 38°W

Through assimilation of T/S profiles, satellite altimetry and radiometric products, G12V1 is already constrained by most observations available in the Tropical Atlantic. A global validation is proposed in the QUID_001_030 report (Drévillon et al., 2018) that shows the overall reliability of this ocean reanalysis. However, currents from surface drifters or ADCPs are not assimilated. Consequently, the drifter-derived surface current AOML climatology is first used to assess the large scale pattern of the G12V1 surface dynamics in the WTNA by carrying out monthly comparisons. Then, taking benefit of the 15 ADCP sections at 38°W, the validation of G12V1 daily estimates is performed along the vertical velocity profiles.

4.1 Validation with the drifters-derived surface current AOML climatology

To be compared to the AOML drifter-derived climatology, the G12V1 1993-2018 estimates of averaged current from 0-15m-depth are monthly averaged to produce an annual mean and 12 monthly climatological means, with a focus in the 15°S-15°N, 70°W-25°W region. The comparison of annual G12V1 and AOML climatologies (not shown) indicates a correct position of the NBC and NBCR, the nSEC, the cSEC and the NECC. In both products, the annual means exhibit the NBCR and NECC connection flowing between 3-10°N, at a location around 6.7°±1.8°N (Fonseca et al., 2004). This NECC annual mean signature presents meandering then latitudinal location on its eastward path relevant with previous descriptions (Garzoli and Richardson, 1989; Garzoli, 1992). For each gridded annual mean current value, the speed ratio (AOML divided by G12V1) and velocity relative angle between AOML and G12V1 are computed (Figures 7a and 7b). On average over the area, the speed ratio is 0.98 (varying between 0.6 and 1.5). Along the main currents (the nSEC, cSEC, NBC, NBCR, and the NECC in the 4.5-7.4°N band) the AOML speed is higher (ratio larger than 1.), with signature of G12V1 being higher at the vicinity (blue band at the edge of red anomalies in Figure 7a). This witnesses a relative lateral shift of these currents among the two products. The relative angle values are on average below 20°, but higher along the edge of the NECC's path. This is confirmed by differences at 38°W (Figure 7c) where larger angle difference appears around 4°N and ratio below/higher than one are visible between 3.5-7.5°N. The NECC's meandering of the annual climatologies are not exactly matching in both products. The AOML products is still assume to be the reference, but it depends locally on the relative distribution of drifters in time in the area, and the interpolation techniques used to produce the climatology.

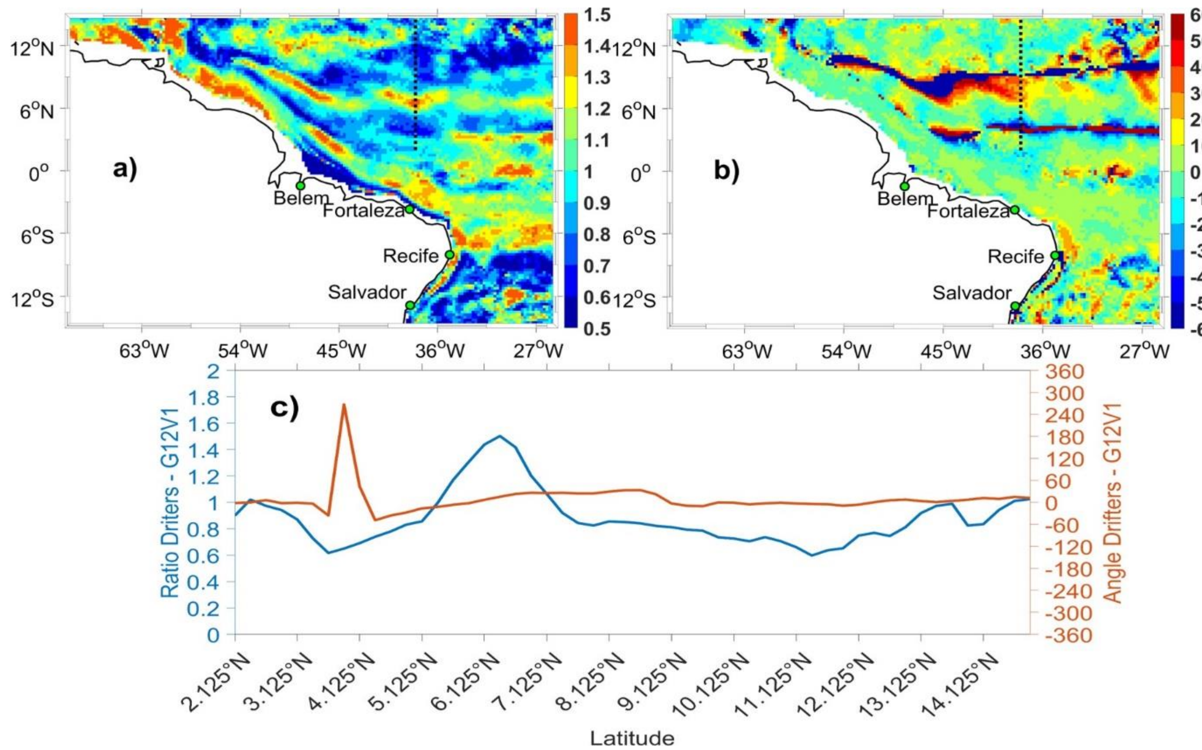

Figure 7. Annual mean currents a) ratio of the speed between AOML and G12V1; b) angle difference between AOML and G12V1 in 15°S-15°N, 70°W-25°W; c) the speed ratio and the angle difference for the section 38°W from 2°N to 15°N, indicated by the black dashed lines on a) and b).

The climatological evolution of the circulation along the year has also been compared between AOML and G12V1 surface currents monthly means by computing root-mean-square differences (RMSD, Figure 8a), speed and angle correlations (Figure 8b and 8c). Both products show the NECC's latitudinal extent between 2-12°N and the northward migration from May/June to October (not shown). Large differences are observed along the NBC, the NBCR, between 1-2°N at position of the nSEC and between 3-5°N, at the position of the NECC. Speed and angle correlations are also lower along the NECC position, the NBC and NBCR. Elsewhere, speed correlations are around 0.5-0.7, showing the overall matching of the AOML and G12V1 seasonal circulation patterns. At 38°W (Figure 8d) speed correlations are higher than 0.5 between 4.5-10.5N, with low RMSD. Angle correlation are also high over 3.5-6°N and 8.5-10°N, indicating that the sNECC and nNECC seasonal positions are matching in AOML and G12V1 monthly climatology. Figure 9 shows the sNECC northward migration from June to November in both climatologies, although the sNECC main position in November/December is shifted southward by about 1° in latitude. From December to March, the sNECC migrates northward from 6 to 9°N, weakens and disappears. In the southern side, from August to

November the nSEC signature remains constant from 2-3.5°N, when the ITCZ is at its northernmost position. From December to May next year, the westward nSEC is growing, shifting northward, and "pushing" the sNECC while the ITCZ is migrating southward. This pattern is matching in AOML and G12V1, although the nSEC signature of G12V1 is too large in July.

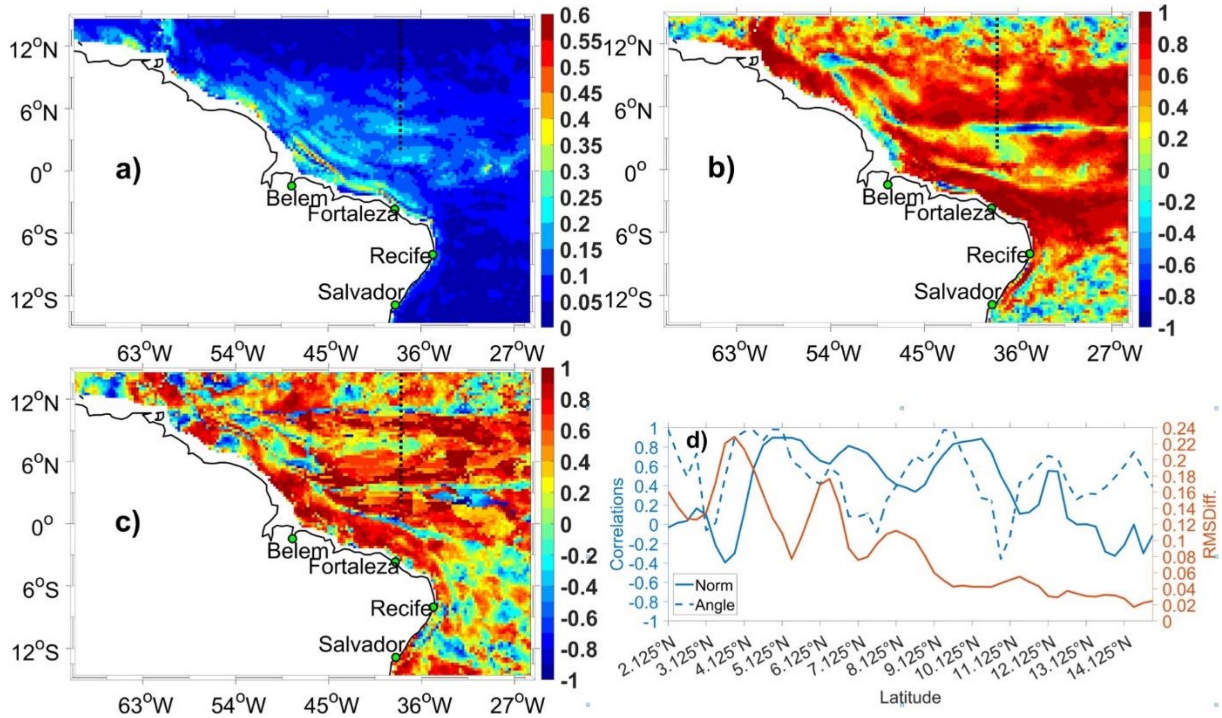

Figure 8. a) Speed RMSD between AOML and G12V1 monthly climatology maps; b), Speed correlation between AOML and G12V1 monthly climatology maps; c) Angle correlation map between AOML and G12V1 monthly climatology maps; and d) Time series of RMSD, speed and angle correlation between AOML and G12V1 monthly climatologies at 38°W. The black dashed lines on a), b), c) indicate the section at 38°W from 2-15°N.

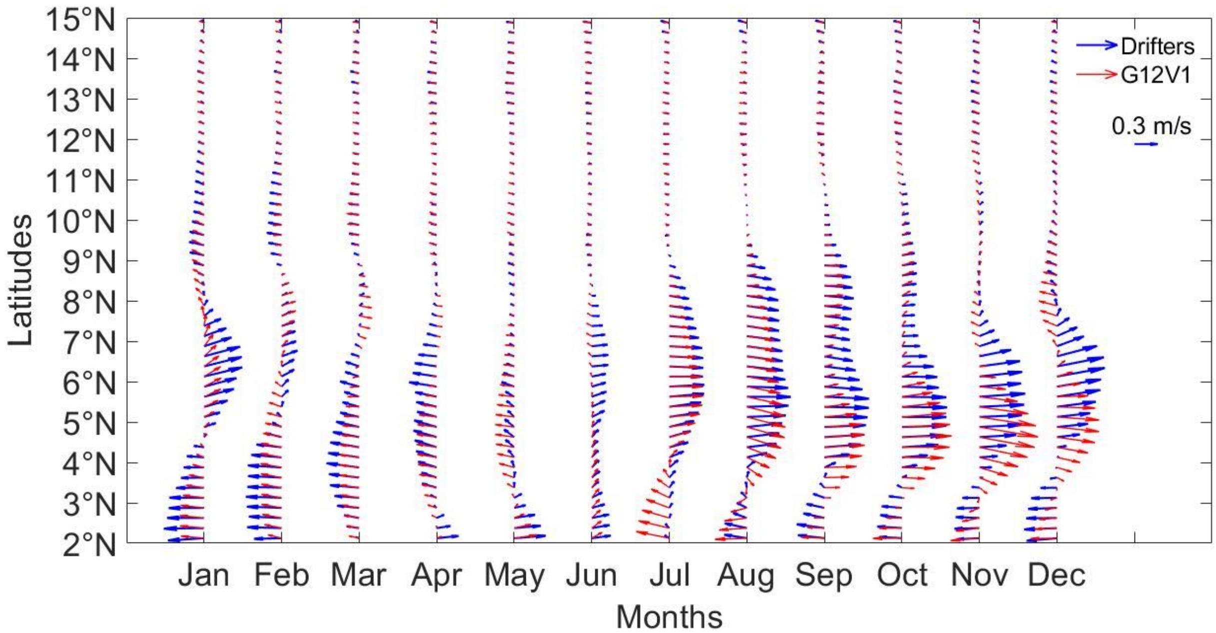

Figure 9. Hovmoller diagram of surface currents at 38°W from AOML drifter-derived surface climatology (blue) and GLORYS12V1 monthly climatology (red)**.**

4.2 Validation with ADCP vertical profiles

Daily G12V1 velocity fields are extracted along the ADCP vertical profiles sections by choosing the closest model profiles to the 15-km ADCP section. From the 15 G12V1 resulting sections, vectorial correlations are computed with the ADCP observed profiles for all valid values along the section and at depth. Vectorial correlation developed by (Vialar, 1978), used by (Rio and Hernandez, 2003) allows to analyze the relationship between the two set of velocities.. In this approach, the correlation coefficient and angle between two vector series are estimated through a least squares method. The total vectorial correlations are larger than 0.5 for most cruises, except in 2001, 2004, 2008 and 2015 (Figure 10). The stretch correlation follows the total correlation, indicating that G12V1 has current intensity co-varying in good agreement with ADCP data. The rotation coefficients indicate overall agreement of currents in the same direction in 2002, 2009, 2011, and opposite directions in 2001, 2012, 2014, 2015. Meaning that instantaneous representation of core currents in G12V1 can be shifted in position (horizontal or vertical) compared to ADCP profiles, even if the overall patterns of the flow are correct.

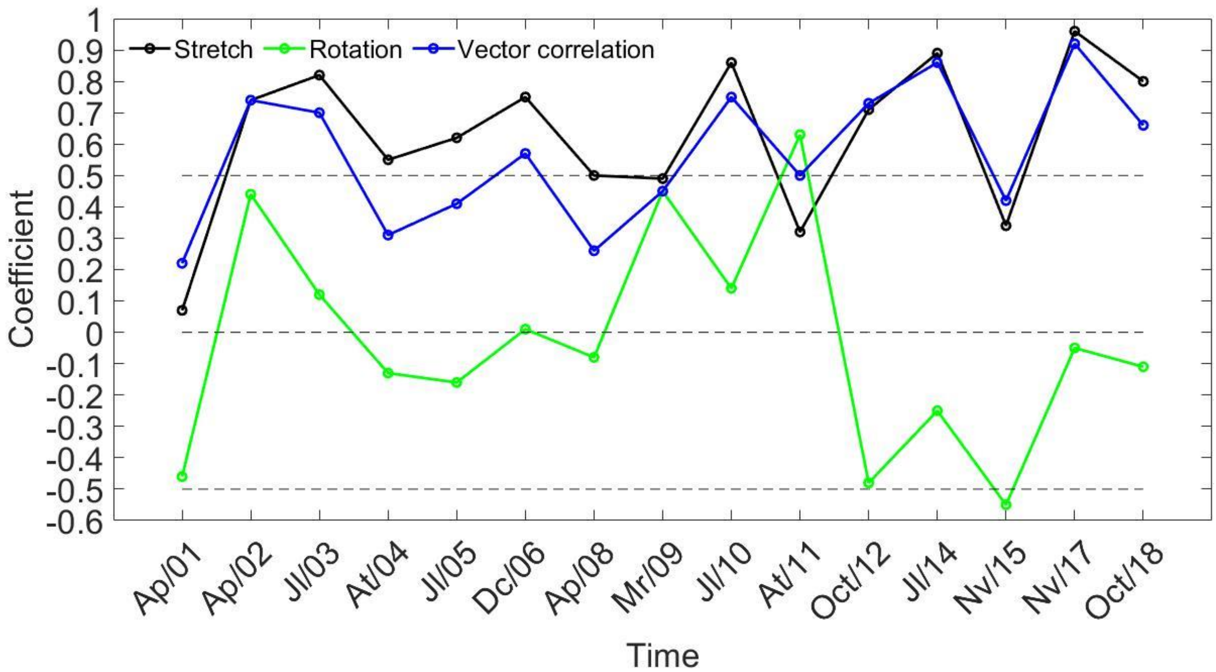

Figure 10. Vectorial correlations between G12V1 and ADCP profiles for the 15 cruises. Total vectorial correlation (blue), stretch (black), and rotation (green) coefficients.

Hence, an alternative comparison is performed in order to characterize the NECC patterns based on four parameters: the presence or not of the two branches, the core current maximum velocity, the latitude and depth of this core. The Figure 11a shows the latitudinal coverage of the two branches from G12V1 and ADCP estimates. G12V1 match the 2 branch-pattern observed by the ADCP profiles. The NECC branches are located between 2-13°N in agreement with Urbano et al. (2006). The sNECC is observed at every cruise in both dataset. The overall latitudinal coverage differences are of the order of 30km. That is, three horizontal grid points of G12V1. For Spring cruises, the G12V1 sNECC can be larger or located more northward, but in April 2008. For July cruises, G12V1 sNECC extension is matching the ADCP, but in July 2003 when it is narrower. During the October-November period, the ADCP data show a sNECC branch extended slightly northward. The nNECC appears in the ADCP and G12V1 in 2003, 2004, 2005, 2006, 2010, 2015, 2017 and 2018. In 2012 the ADCP section is too short to measure the nNECC present in the G12V1 estimates. The nNECC latitudinal extensions appear larger in G12V1, but in 2005. The overall latitudinal coverage differences of the G12V1 nSECC is less than 30km with regard to the ADCP sections. Comparison of the depth of NECC's branches core and maximum velocity (Figure 11b) show the overall agreement in term of NECC's intensity and vertical extent. RMSD of core's depth location and intensity between G12V1 and the ADCP observation is about 7 m and 0.12 m/s; and 12m and 0.06 m/s for the sNECC and nNECC respectively. For cruises with the 2 branches, the depth errors are of the same order for both branches, which indicates that the vertical structures represented by G12V1 are consistent. However, the errors on core's maximum velocity do not present any obvious scheme. The nNECC maximum core velocity is lower than for the sNECC, but errors are not relatively smaller.

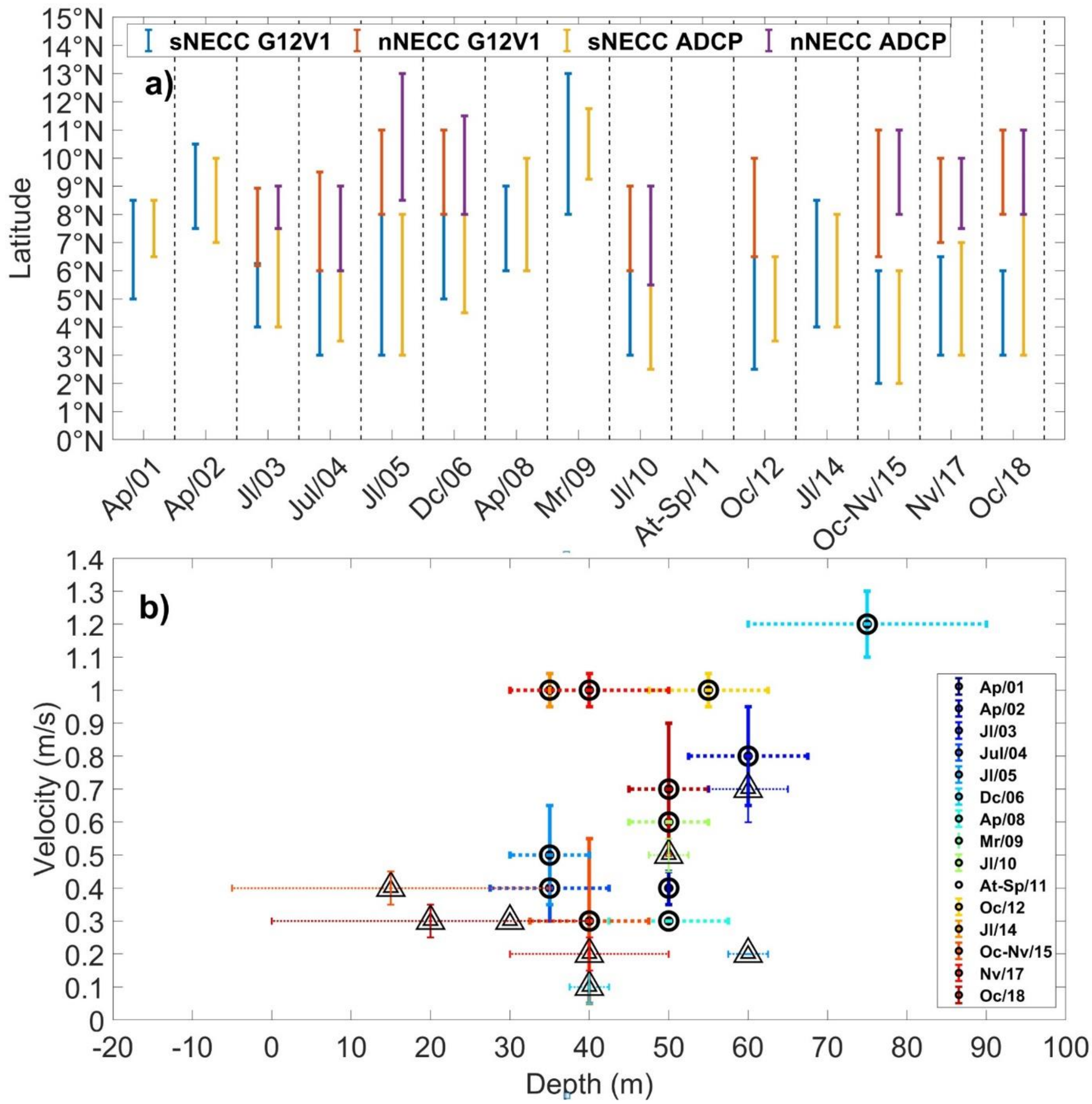

Figure 11. NECC comparison between GLORYS12V1 and ADCP for the different cruises: a) latitudinal coverage of NECC branches from ADCP and GLORYS12V1; and b) depths and maximum velocity of the NECC branches core. Colors are associated with each cruise. Central point of each cross corresponds to the ADCP estimates of these two parameters (circle for the sNECC and triangle for the nNECC). The horizontal error bar (dotted line) is the depth difference of G12V1 with respect to ADCP estimate. The vertical error bar (solid line) is the velocity difference of G12V1 with respect to ADCP estimate. The thick and thin lines correspond respectively to the sNECC and nNECC estimates.

In addition, the transports associated with the NECC branches are computed for three vertical integration depth (30m-depth to 100, 150 and 200m-depth), then compared between G12V1 and ADCP estimates. NECC and sNECC transports show correlation of 0.6 to 0.9, that reach 0.94 for the 30-150m-depth integrated value, and RMSD about 4.5 Sv, for transport values ranging from 2 to 20 Sv (Figure 12). Transports for the nNECC are smaller, ranging from 1 to 10 Sv. Their representation by G12V1 is less reliable than for the sNECC, in particular at depth: correlations with the ADCP data are lower. and higher near the surface (30-100m) than deeper (30-200m). RMSD range from 2.1 (30-100m) to 3.4 Sv (30-200m). So, it appears that compared to ADCP measurements, G12V1 provide reliable transport estimates near the surface and overestimate the transport below 150m-depth.

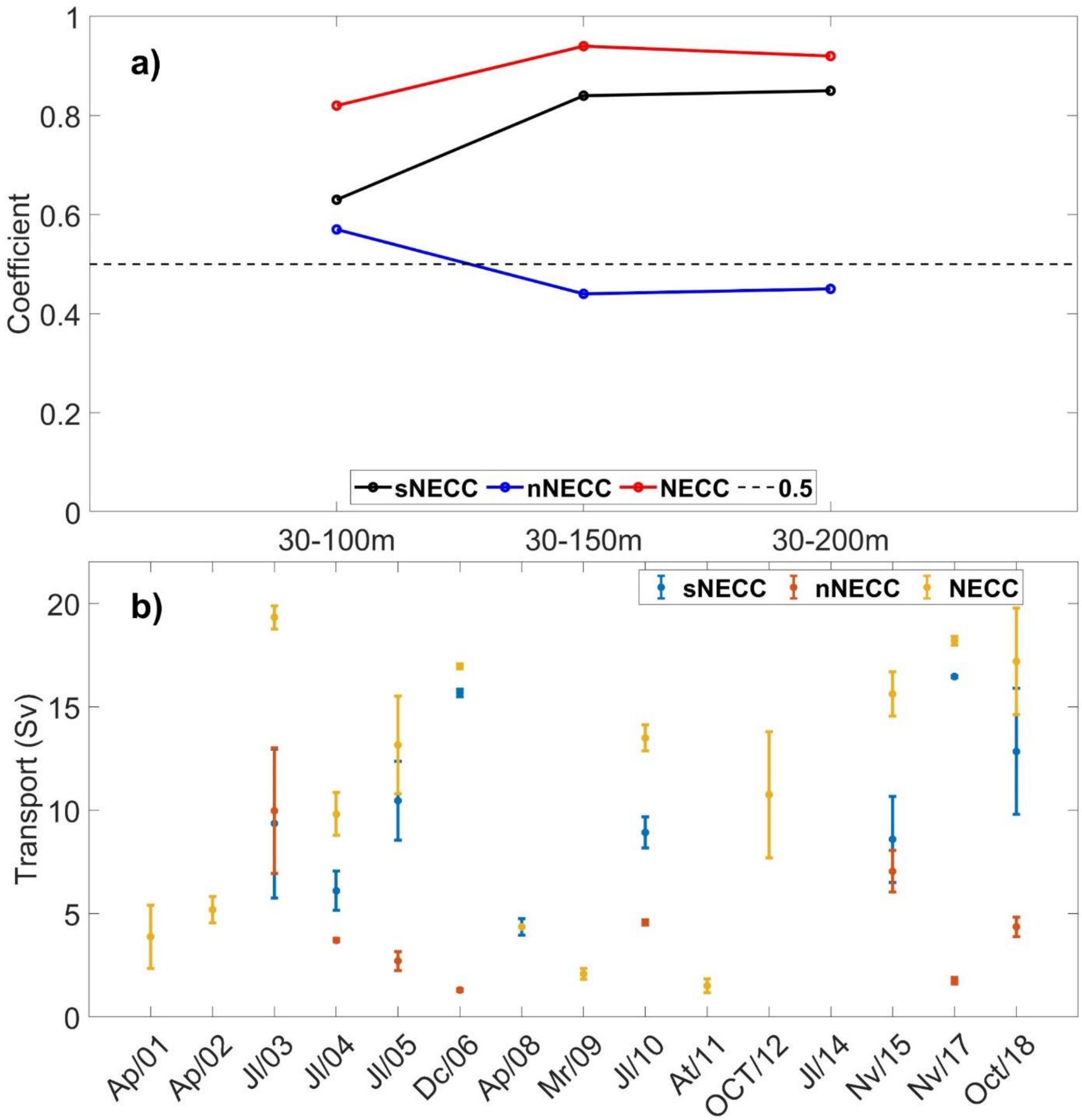

Figure 12. Comparison of NECC's branches transport between G12V1 and ADCP data (in Sv): a) correlation of sNECC, nNECC and NECC for the integration depth from 30-100, 30-150 and 30-200m-depth; and b) the transports 0-150m-depth of NECC branches (total NECC in yellow, sNECC in blue, nNECC in red) for the 15 ADCP cruises. The point represents the ADCP transport value, the error bars correspond to the difference with the G12V1 estimates.

In conclusion, G12V1 is worthy to be considered for further analysis of the near surface circulation in the WTNA, and provide a valuable description of the NECC dynamics and variability.

5 Analysis of the NECC variability using the GLORYS12V1 reanalysis

5.1 Seasonal variability of the NECC and the relationship between its transport and the ITCZ at 38°W

To investigate the temporal and spatial variability of the NECC, the G12V1 monthly climatology is computed over the 1993-2018 period along the 38°W section covered by the ADCP data (Figure 13). This climatology confirms the description of the NECC's annual cycle presented at section 3. The NECC flows between 3-12°N during the year, separated in two branches from July to November. The sNECC extends between 3-10°N on average at 6°N±1.2°, at a mean depth of 47±6m. The nNECC is located between 6.5-12°N, on average at 8.3°N±0.8° at a mean depth of 39±5.3m.

The NECC annual cycle can be consider with a start in June. The EUC extends toward 4°N, shallowing, and connecting at 75m-depth with the upper part of the NEUC. The NEUC, lying between 4-7°N, presents its maximum intensity, with a core at 175m-depth and 0.5 m/s. The shallowing of the NEUC and wind forcing by the ITCZ northward migration generate the eastward surface flow giving birth to the sNECC (Urbano et al., 2006). There is still the remnant nNECC branch at 9°N of the previous year that finishes its northward migration and vanishes. The new sNECC grows at the surface and migrates northward in July with a small second velocity core at its northern side that appears under the influence of the ITCZ northward migration with a 3-month lag (Figure 14). In August, the northern edge of this growing and extending sNECC to the north witnesses an independent vertical extension at 8-9°N: the northern core is becoming the new nNECC. The entire NECC system continues its northward extension until November when the new nNECC fully separates from the sNECC, that has been keeping is position lying around 4-6°N, extending vertically and merging with the NEUC. The nNECC is still migrating northward due to the 3-month lag influence of the ITCZ until December when it vanishes around 11°N. From November to next year in April, the sNECC migrate northward extending between 7-9°N, under the influence of the wind stress curl second zero crossing that appeared again in November (Figure 14). At the same time, on the southern side, the EUC is shallowing and extending northward, and the nSEC also shifts northward, and expands with its maximum intensity. At depth, in April the sNECC feeds the EUC underneath at 50m. The circulation map at 50m-depth in April (Figure 15a), shows that the sNECC bifurcates around 36°W, and generates the flow westward (observed at 38°W between 3-6°N) that recirculates eastward around 45°W to feed the shallowing EUC, that exhibit maximum transport at this period of the year (Hormann and Brandt, 2007). The NEUC appears again vertically independent from the northward migrating sNECC in February. It intensifies and connects to the EUC in May. Then in June this shallowing EUC and NEUC flows feed a brand new NECC (Figure 15b).

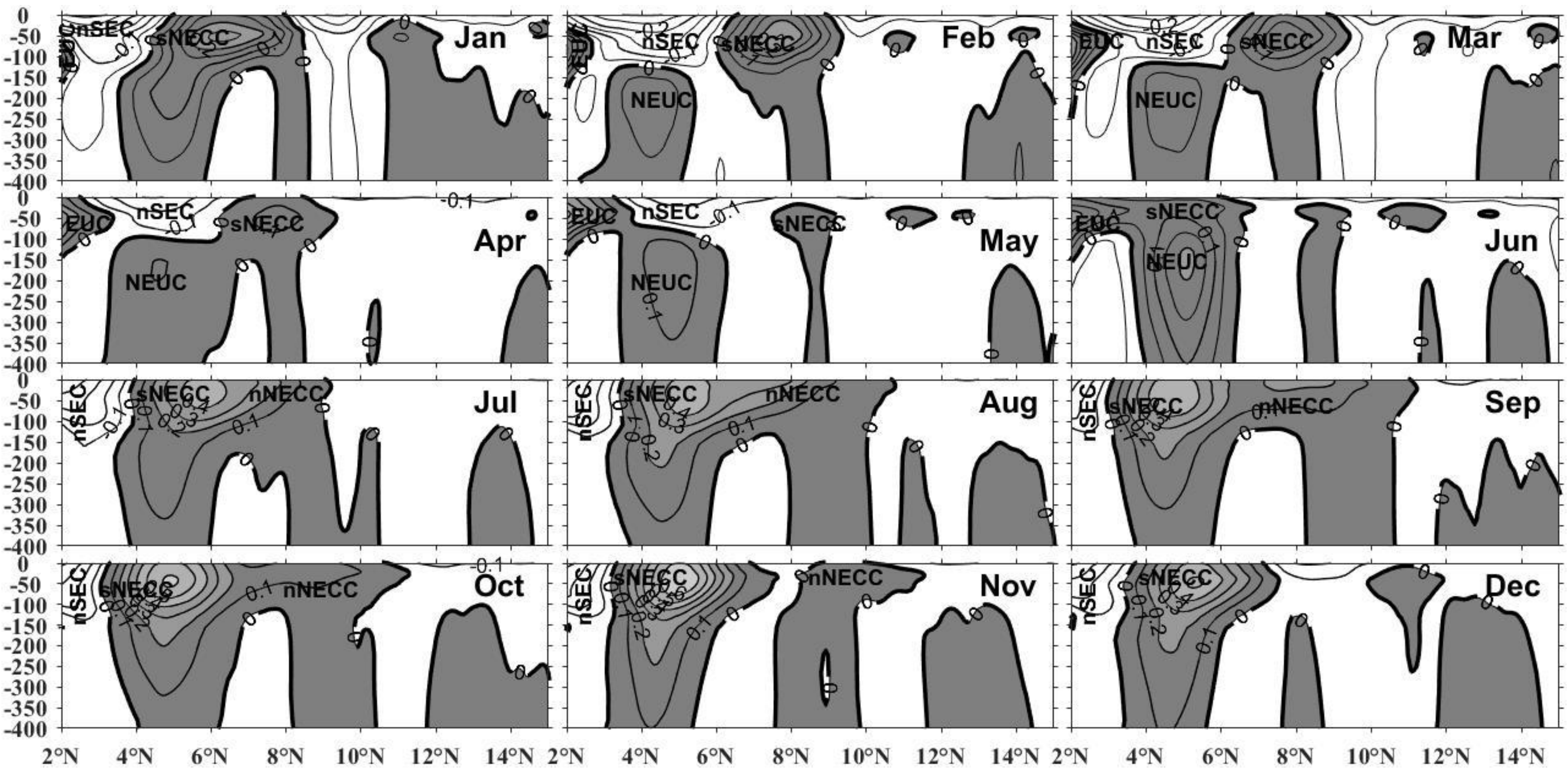

Figure 13. G12V1 monthly climatology of zonal current at 38°W between 2-15°N. Shaded gray and white areas represent respectively the eastward (positive) and the westward (negative) velocities with contours each 0.1 m/s. The zero-contour in black thick line.

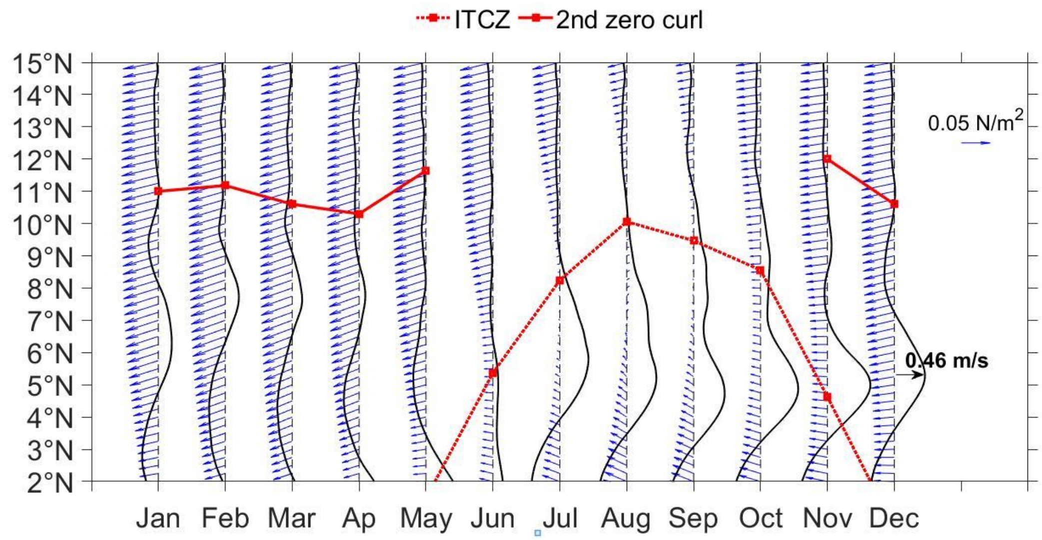

Figure 14. Hovmoller diagram of 0-100m vertical averaged currents from G12V1 monthly climatology at 38°W (black lines). The thin dashed line plotted each month is the zero value of currents, westward/eastward flow resp. on the left and right side. Wind stress influence on currents is given by ERA5 monthly wind stress at 38°W (blue arrows). ITCZ latitudinal position at 38°W (red dotted line with square). The second zero crossing at 38°W of the wind stress is indicated in red thick lines and circles.

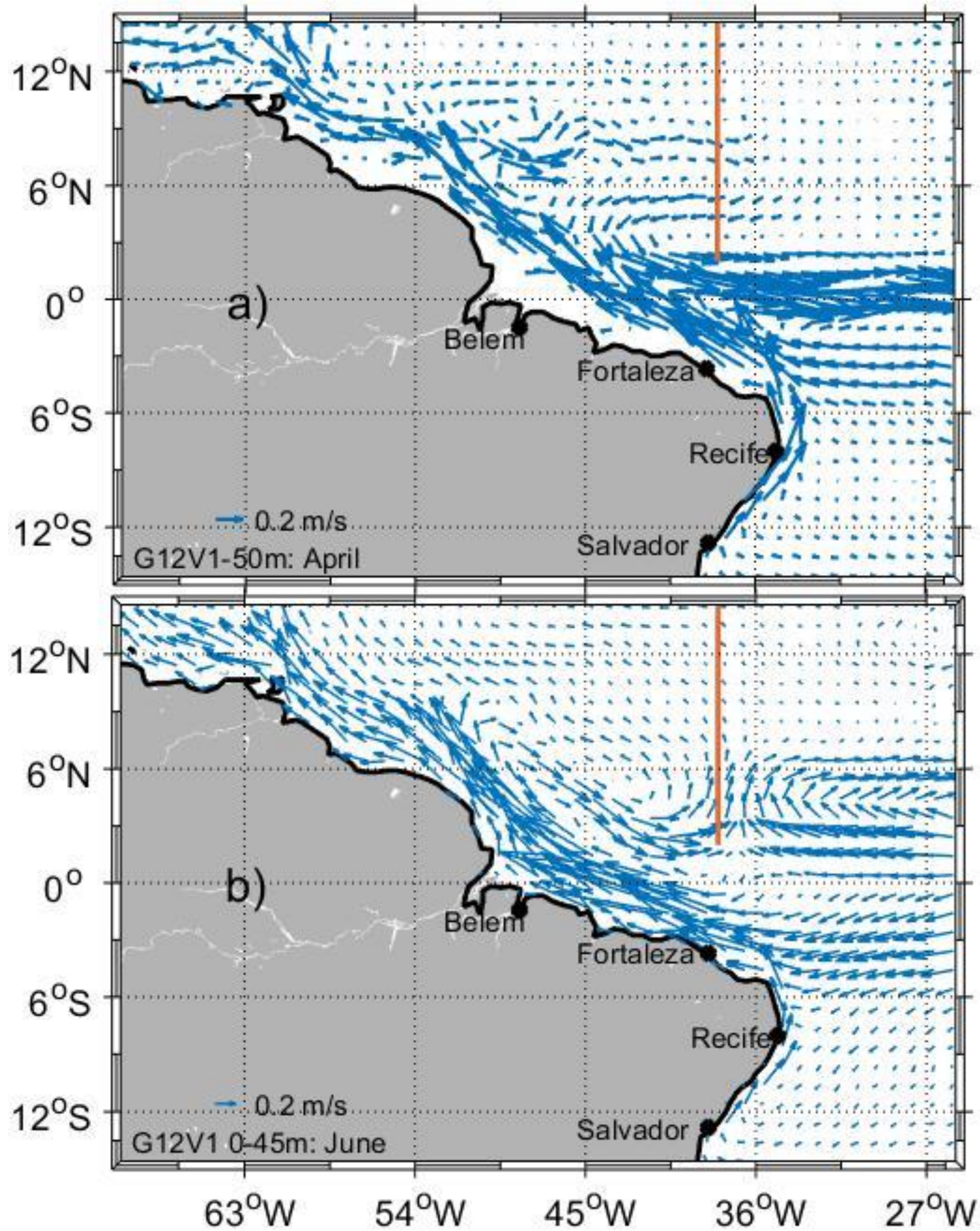

Figure 15. G12V1 monthly climatology of currents in the region 15°S-15°N, 70°W-25°W: a) around 50 m; and b) from the surface to 45 m. The orange line indicates the section at 38°W between 2-15°N.

This NECC annual cycle is summarized in term of transport by Figure 16. The total NECC integrated transports grows from 1 Sv in May to 22 Sv in October, following the ITCZ northward migration with a 3-month lag. From July to November, the nNECC transport contributes to 2.8 Sv to 10 Sv to the total eastward flow.

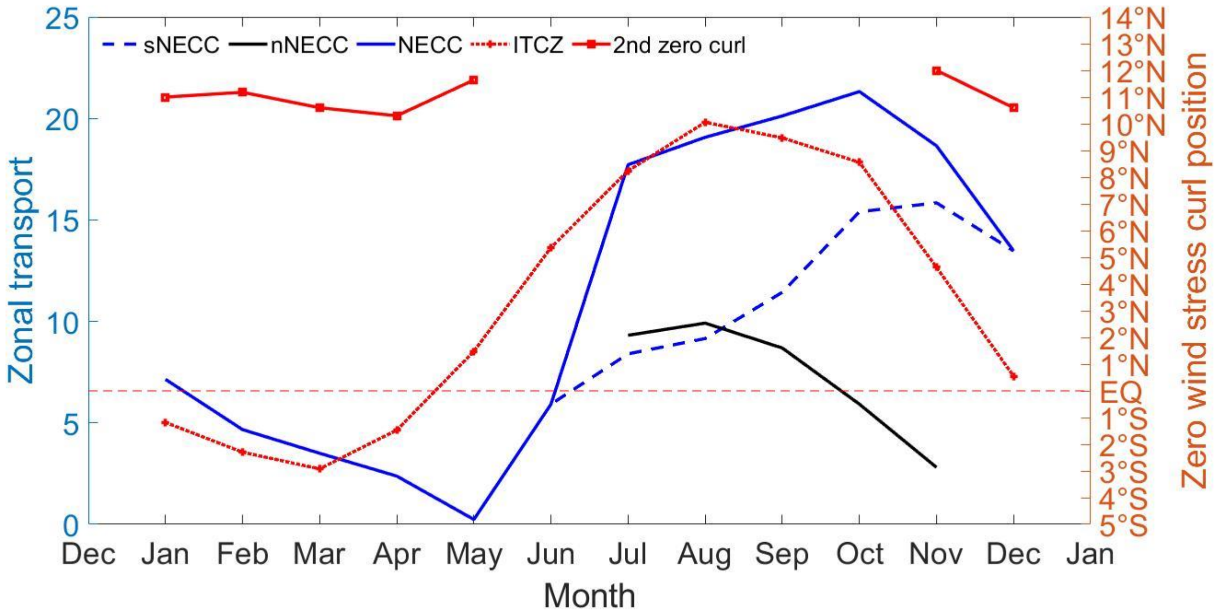

Figure 16. Annual cycle at 48°W of the G12V1 NECC transport (blue, in Sverdrup) and of the ERA5 wind stress curl zero-crossing locations (red in degrees of latitude). Total NECC transport in blue dashed line with circles. sNECC transport in blue solid thick line. nNECC transport in blue solid thick line with circles. Wind stress zero crossing corresponding to the ITCZ in red dotted lines. Second wind stress zero crossing in red solid thick line.

5.2 Interannual variability of the NECC and its relation with the Atlantic modes at 38°W

The monthly estimates of current at 38°W from G12V1 are analysed in order to infer the interannual variability of the NECC. Year to year variability is significative. A maximum 0-150 m-depth NECC transport of 32.2 Sv is estimated by G12V1 in October 2012, while it can vanish or quasi disappear some years in April or May. Mean value of the transport in May/October is respectively of 1.3±1 / 24±4 Sv. In terms of anomalies against the seasonal cycle, it can account positively or negatively for more than 10 Sv, representing 75% of the mean transport (13.3 Sv) from 1993 to 2018.

The first 15m-depth averaged velocities are computed from 1993 to 2018 (Figure 17a), as well as anomalies against the seasonal climatology (Figure 17b). For sake of clarity, anomalies are plotted only where the NECC is observed (eastward positive values in Figure 17a). These time series show the NECC interannual variability, with an average location at 6°N (dashed line in Figure 17). Around this latitude, the NECC is strong the second half of the year in 1994, 2000, 2007, 2011, 2013, 2014, and 2017. The sNECC appears every year south of this mean latitude, with approximately equal occurrence of strong/weak anomalies over years. The two-core structure is visible the second half of the year, with interannual variations. There is no evidence of nNECC remnant pattern from on year to the other, at the opposite of Urbano et al. (2008) hypothesis. Although, in 1995-96, 1999-00 and 2012-13, north of 10°N, the anomalies exhibit a stronger nNECC extending northward. More south, the previous year's sNECC branch can be visible during spring (in 1995, 1997, 1999, 2001, 2005, 2012, 2017 and 2018). Then connects between 7-9°N with the northward migration of the new sNECC and enhance the growing nNECC branch in July-August. The northward propagation of the sNECC feeding the nNECC from August to next April is particularly visible in 1994, 1998, 2001, 2004, 2014, 2015 and 2017.

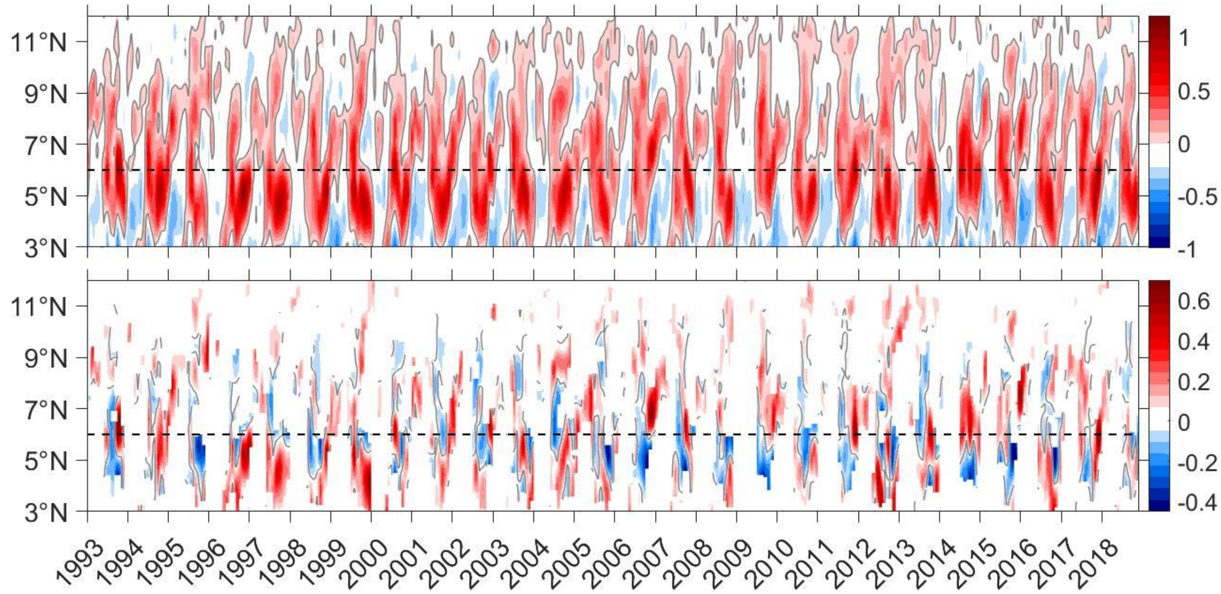

Figure 17. Hovmoller diagram of the total zonal velocity averaged between 0-15m at 38°W (top) and its corresponding seasonal anomalies over the years (bottom). The horizontal dashed line represents the NECC maximum velocity mean position. The zero contours velocity appears in grey lines.

To investigate the relationship between this NECC interannual variations and the coupled ocean-atmosphere variability in the tropics five parameters are taken into account. First the monthly NECC transport seasonal anomalies in the first 150m-depth at 38°W computed with G12V1. Second the Atlantic Zonal Mode index (AZM) based on NOAA OI SST seasonal anomalies in the ATL3 box, defining warm events and the so-called "Atlantic Niño" (Zebiak, 1993). Third, the Atlantic Meridional Mode index (AMM) dicussed by e.g., Carton et al. (1996); Foltz et al. (2012); Servain (1991), and computed here using the NOAA OI SST anomalies over the Tropical North Atlantic (TNA) and Tropical South Atlantic (TSA) boxes as defined by Enfield et al. (1999). AMM's positive/negative phases are associated with respectively opposite warm/cold events in the TNA/TSA and anomalous northern/southern latitudinal shift of the ITCZ (Cabos et al., 2019). Fourth the monthly ITCZ position seasonal anomalies (hereafter ITCZ index) based on the location of the minimum ERA5 wind stress meridional component. And fifth, the meridional ERA5 wind stress seasonal anomalies at 6°N/38°W (hereafter WS6 index). Wavelet analyses of these five time series (not shown) indicate that interannual variability appears at periods larger than 2 years, reason why they are first analysed and presented at Figure 18 after applying a low-pass filter with a 24-month Loess filter (Cleveland and Devlin, 1988). In parallel, to identify when maximum interannual variability occurs within each year, the monthly time series are just three-months averaged to generate time series from 1993 to 2018 for each season.

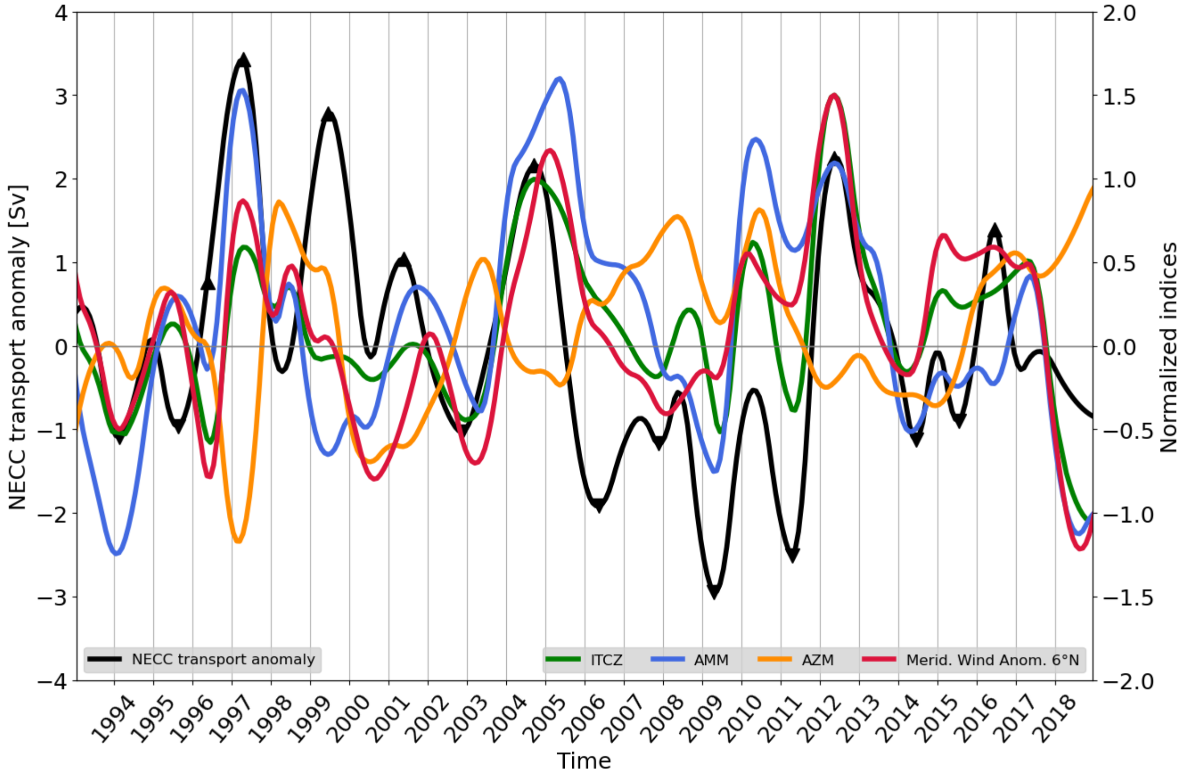

Figure 18. Low-pass filtered time series. The NECC transport anomalies against the seasonal cycle (black, units in Sverdrup, scale on the left axis), with anomalous years indicated by triangles. Then tropical Atlantic modes indices: AMM (blue) and AZM (orange). ITCZ index (green) represents the seasonal anomaly of the ITCZ position at 38°N. WS6 index (red) corresponds to the seasonal anomaly of wind stress at 6°N/38°W. Scale for the 4 indices on the right axis, all values are normalized.

Figure 18 shows AMM and AZM time series with visible anti-correlation, in agreement with the opposite extreme events in 1997, 2005 and 2008 mentioned in Hormann et al. (2012). The ITCZ index witness positive/negative annual correlations with the AMM/AZM index (0.65 / -0.5). Three-months averaged time series correlations are larger (0.7) during the March-May then Sept-Dec period, with one month lag with the AMM index as already documented (e.g., Cabos et al., 2019). These periods correspond to the start of the ITCZ northward migration after boreal winter, and during the southward migration of the boreal summer ITCZ northern position. The WS6 index presents also positive annual correlation with the AMM index (0.55), with higher correlations during the April-June (0.7), and the Sept-Dec (0.6) periods. The ITCZ index witness significative anti-correlation (-0.7) with the AZM index only for the March-July period, with one month lag also, when the ITCZ migrates from its southern to northern bounds. Annual correlation between the WS6 and AZM indices are less significant. However, negative correlations (-0.65) are observed for the three-months averaged time series during January-June period, which indicates its influence when the North Easterly Trade Winds diminish to let the place of the South Easterly regime. Again, this is in aggreement with the known negative impact of positive AZM phase on Trade Winds in the WTNA (Cabos et al., 2019).

Hence, AMM and AZM combination of positive/negative phases can be related to the ITCZ and associated wind pattern (WS6 index) interannual variability, and consequently to the

NECC system variability observed in Figure 18. The filtered interannual variations of the NECC transport show remarkable positive anomalies occurring with northern anomalous positions of ITCZ. In particular in 1997, 2004 and 2012 during AMM warm and AZM cold phases, and positive WS6 index. In 2001 the NECC transport positive anomaly, weaker, is also associated with positive/negative AMM/AZM, with a ITCZ index local extremum and a negative but increasing WS6 index. At the contrary, in 1999 and 2016 the NECC positive transports occur during positive AZM and AMM negative phases. Negative peaks of NECC's transport anomalies present less consistency with other indices. In 1994 and 2009, the AMM index is negative, and the AZM index is either slightly positive or negative, but finishing the year into a positive tendency, the ITCZ, WS6 indices are negative. This pattern is less clear for 1995 (AMM, AZM positive phases, ITCZ, WS6 indices slightly positive) and 2011 (AMM, AZM positive on decreasing phases, ITCZ negative, WS6 positive with local minima). During the 2006-08 period, the NECC transport is negative, and associated with the variations of the a pluri-annual positive AZM phase, a negative WS6 index, while AMM changes from positive to negative values along the period, with a local minimum in conjonction with the ITCZ index. Hence, from 1993 to 2018, a robust pattern appears with positive (negative) NECC transport occurring when ITCZ is anomalously north (south) of its normal position, or when ITCZ changes exhibit positive or negative local extrema. In such pattern, positive NECC transport occurs when the AZM is negative, or positive and decreasing. While negative NECC transport occurs merely when the AZM is positive, or zero but increasing.

Now if we analysed unfiltered time series (not shown), we see first that dominated by the seasonal cycle, the NECC transport correlations are strong (0.9) with both the ITCZ and WS6 indices, with one month time-lag. At interannual time scales with annual average time series comparisons, the NECC transport anomalies present low correlations with both the AMM and AZM indices. However, three-months averaged time series correlations are significant (0.5 to 0.7) between the NECC transport anomalies from January to May and the AMM index with one month lag. In a consistent way with the correlations between the ITCZ, WS6 and AMM indices, the NECC transport in March to May appears significatively correlated (0.55 to 0.75) with the ITCZ and WS6 indices at the same time. Then very significantly anticorrelated in April to June (-0.65 to -0.75) with the AZM index in April. In other terms, the climate mode influence seems more pronounced during the first part of the year, when the NECC system presents its weakest transport (Figures 13 and 16). By the way, the previous section stated that the NECC system seasonal pattern is formed by the evolving sNECC and nNECC branches. Reason why time series of sNECC and nNECC transports, location, core intensity, latitude and depth are computed (Figure 19) and analysed in relation with the climate indices.

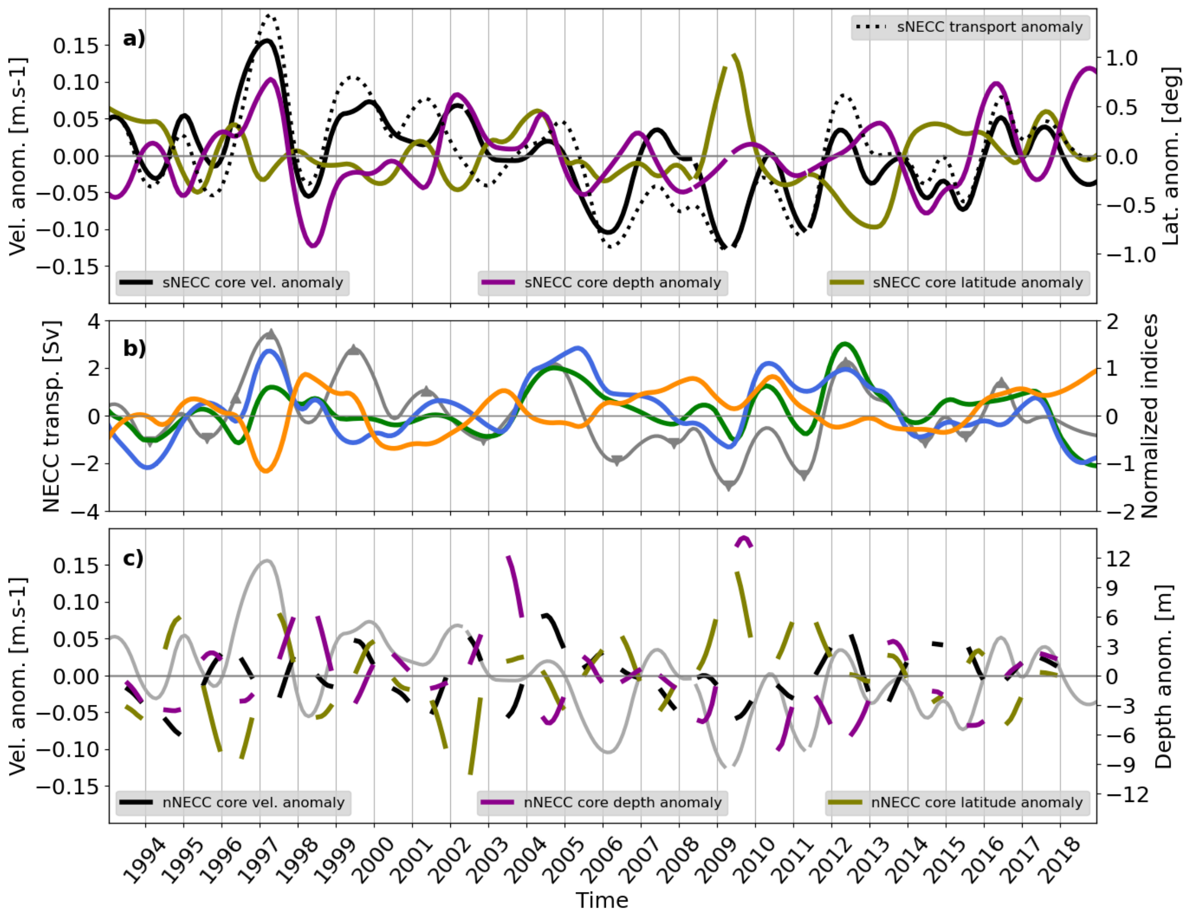

Figure 19. Low-pass filtered time series: a) sNECC interannual anomalies of core velocity (black, units in m/s, scale on the left axis), core depth (dark magenta, units in meters, scale on the right axis of Figure c) below), core latitude (olive, units in degrees, scale on the right axis) and sNECC transport anomalies (dotted black line, unites in Sv, scale given on the left axis of b) below); b) AMM, AZM and ITCZ indices reported from figure 18 (normalized scale on the right axis). The dark grey solid line corresponds to the NECC transport and anomalous years (triangle) of figure 18 (units in Sv, scale on the left axis); and c) same as a) for the nNECC. The dark grey thin solid line corresponds to the sNECC core velocity anomalies plotted in black above in a).

The sNECC transport and its core intensity are naturally correlated (0.90), with similar seasonal cycle minimum/maximum in respectively May/November (less than 0.15 and more than 0.8 m/s). Figure 19a shows that this relationship remains at interannual time scales, with correlation larger than 0.75, larger than 0.85 for most seasons, but in May to July, when a new sNECC branch starts. At the opposite, there is no obvious correlation between the sNECC transport and its depth, unless at interannual time scales in May: a correlation of 0.5 showing that when the sNECC ends/starts a new cycle, its depth might be partially linked to the transport values the previous January to April (i.e., deeper core in May associated with larger transport the previous months). The sNECC core latitude exhibits a robust seasonal pattern (Figures 13 and 15): starting from June to January where it occupies a position between 4-6°N, when the transport is larger, then shifting northward to 8-9°N from February to May with a decreasing tranport. At interannual time scales, again, the only remarkable correlation (0.50) of the sNECC core latitude appears in May and June, with the transport anomaly from February to May: the latitude of the ending/starting sNECC branches linked to the transport values the previous month (i.e., northern sNECC core position in May-June associated with larger transport the previous months). The sNECC transport from December to April appears anticorrelated (-0.5 to -0.6) with the AZM index at the same time or with one month time lag, while in June and July it appears anticorrelated (-0.65) with the AZM index in Feb-May. This is also shown on Figures 19a-b where the sNECC's core velocity appears negatively influenced by the AZM: the negative (positive) AZM values are associated with positive/decreasing (negative/increasing) anomalies of the sNECC core velocity. sNECC transport and core velocity show correlations with the AMM index (0.4 to 0.6) between March and May with one month time lag, consistently with correlations with the total NECC transport mentioned above. For this period, correlations are more significative (0.5-0.7) with the ITCZ and WS6 indices. The same pattern also appears for the sNECC core location. In other terms, during AMM positive phase and when the ITCZ northward shift is more pronounced associated with south-easterly wind tendency, the sNECC has a larger transport and it occupies a northern position. The opposite pattern appears for the sNECC branch the second half of the year: negative correlations (-0.5 to -0.6) between the sNECC core location and the AMM and the ITCZ indices, meaning that AMM positive phase with ITCZ north-than-normal position are associated with a sNECC branch from August to December shifted southward.

The nNECC seasonal pattern initiates with a branch detaching from the sNECC around June at 7°N, migrating northward to 10-11°N until december, with a maximum transport of 6.5 Sv in September (Figures 13 and 15), associated with a maximum core intensity around 0.3 m/s. Again, the core velocity follows the transport strength (0.75 correlation on full time series). Its core depth is shallower in August-September (10-20m), when the transport is maximum, then deepens below 35 m in December. At interannual time scales, nNECC transport and core velocity are also significatively correlated (0.6), with correlation exceeding 0.9 from October to December: year to year, the nNECC core intensity follows the nNECC branch transport strength, particularly during its decaying phase and northward shift. The nNECC core depth appears only correlated (0.65) with the transport from June to August: larger the transport of the beginning nNECC branch, deeper its core. The nNECC core position appears also correlated to its transport: it occupies in June to August a northern position when its transport is stronger in June. During its decaying phase (Nov-Dec), the nNECC position and transport correlation is higher (0.8), indicating that stronger the transport, more north the position of the nNECC. Considering the Atlantic climate modes, we do not notice significant relationship between the nNECC caracteristics and the AZM index (Figures 19b-c), while some relationships appears with the AMM, ITCZ and WS6 indices, with respectively correlations of 0.5, 0.6 and 0.4 on average with the nNECC transport anomalies. A more robust pattern appears over the three-months averaged statistics. The Nov-Dec nNECC transport, core intensity and position are correlated (0.5-0.7) with the AMM index in Aug-Oct, with the ITCZ index (0.5-0.8) with one month lag, and with the WS6 index (0.6-0.7) with no lag. In filtered time series (Figures 19b-c) southward shift of the nNECC associated with AMM negative or decreasing phase are visible in 1993, 2000, 2002, 2007, 2014 and 2016.

To finalize this statiscal analysis, the relationship between the sNECC and nNECC branches and caracteristics are analysed. The Figure 19c exhibits associated patterns between the sNECC core velocity and nNECC core latitude, with common tendencies for most year. Hence, indicating a relation between the sNECC intensity and the nNECC northward migration. In 1993, 1995, 1998, 2004, 2014 (respectively 1995, 1997, 1999, 2012) negative (positive) anomalies are associated to positive (negative) anomalies of the nNECC core latitude. A particular case of a remarkable positive anomaly is also noticed in 1997 during the decaying phase of the sNECC core velocity. Hence Figure 19c suggest that a weaker (stronger) sNECC is associated with a nNECC positioned northward (southward). Three-months averaged time series statistics indicate that over years, a significative anticorrelation (-0.6) appears between the sNECC and nNECC transport in July-August. Then we notice anticorrelation (-0.5) in Nov-Dec between the sNECC core velocity and the nNECC core position; and between the sNECC core velocity in June-July and the nNECC core depth in September. Which confirms that the sNECC pattern influences the nNECC shape during and after its detachment. The sNECC transport is mostly influenced by the AZM from December to July, and very less significatively by AMM during the second phase of the year. While positive phase of the AMM are significatively related to nNECC strength and position in August-September. We might witness some years the dual influence of the AMM both on sNECC strength and nNECC position from June to December.

6 Discussion

Comparisons of G12V1 seasonal circulation in the WTNA with the NOAA drifter derived surface velocity climatology exhibit strong similarities. Moreover, synoptic comparisons with the fifteen ADCP vertical surveys along 38°W indicate that G12V1 reproduces satisfactorily strength and vertical positions of the main cores of the EUC, NEUC, nSEC and NECC's branches. Which ensures that the G12V1 reanalysis offers a reasonable reliability for further analysis.

The NECC at 38°W shows a strong seasonal cycle that can be considered starting in June. It displays a two-core structure from July to October, becoming two separated branches in November (Figures 13, 14 and 16). The NECC's latitudinal extension is found between 3±0.3°N and 12±0.2°N, with its southern/northern branch, sNECC/nNECC extending respectively between 3-9.5°N and 6.5-12°N. After December the NECC system consists in the sNECC branch constrained in its southern flank by the nSEC, and a weak nNECC branch flowing north of 10°N at the vicinity of the NEC, that vanishes later. When the NECC seasonal cycle is going to start (May-June), interactions appear between the EUC that surfaces and connects to the NEUC located more north at depth. Then the NEUC is vertically connecting with the incoming NECC at the surface. Interestingly, we observe that the surfacing and strengthening of the EUC during May-June is partly fed by the southern recirculation of the sNECC in April (Figure 15). In agreement with Fonseca et al. (2004); Urbano et al. (2008) the NECC system presents two migration periods (Figures 13, 14 and 16). The first period from June to November corresponds to the growth of the NECC transport in conjunction with the ITCZ northern migration with a three-month time lag (Figure 16) , associated with the time of Rossby waves propagation from Africa, and related to the delayed response of transport above the thermocline with the wind stress curl forcing (Garzoli and Katz, 1983; Urbano et al., 2008). The second period, from November to April, is under the influence of the second zero of the wind stress curl (Figure 14) that induces also a northward extension of the nSEC becoming larger and deeper. The sNECC shifts northward from December (extending from 3.5 to 6.5°N) to May (around 8-10°N). But contrary to Urbano et al. (2008) it is evidenced that when the sNECC weakens in May and the new NECC cycle is initiated, some years, this remaining sNECC branch may possibly become the nNECC signature which remains north of 9°N until it merges with the newly forming nNECC branch migrating northward the next year. However, we confirm their hypothesis and the role of the wind stress second zero crossing, responsible for the sNECC northward migration, intensification then decay from January at 5°N to April at 9°N. The sNECC mean position is found at 6±1.2°N in agreement with estimations at 6°N by Hormann et al. (2012) and (Fonseca et al., 2004); and has a core maximum velocity of 0.7 m/s in November around 5°N (Figure 13). But in contrary with Urbano et al. (2008) who found maximum in September using the geostrophic zonal near-surface velocity from drifters. To summarize seasonal position of the NECC system, the sNECC has two northernmost positions in May and February respectively around 8.8°N and 8°N and two southernmost in June and September respectively around 4°N and 4.7°N. The nNECC begins in June around 7.3°N then migrates northward around 10.4°N in November-December. Fonseca et al. (2004), based on satellite altimetry, considering the NECC as a unique branch, found also two southernmost positions: in June and December, around 4°N and 5°N respectively. Then two northernmost positions: in February in agreement with present results, and in August, both around 7°N. This last estimate indicates that the nNECC pattern might have been loosely captured by satellite altimetry in their study. Absolute depth estimation of nNECC and sNECC cores based on G12V1 might be more questionable, as discussed with Figure 11b (7 and 12m-depth error for respectively the sNECC and the nNECC). However, a seasonal pattern can be inferred. The sNECC (nNECC) follows a seasonal cycle with a maximum of 55 m-depth (36m) in February (December) and a shallower extension of 34 m-depth (12 m) in July (August). This depth seasonal cycle can be associated with core's intensity. Inversely proportional for the nNECC, with a weaker/stronger core related to a deeper/shallower depth. The opposite occurs for the sNECC branch. Both core velocity and depth have same tendency: intensifying and deepening from June to December under the influence of ITCZ, then weakening and shallowing from January to May. The sNECC core deepening from July to October-November can be related to the Rossby waves that deepens the thermocline. Hence, the sNECC core depth in this period can be used to characterize the thermocline depth variations.

For the first time, the volume transport of the two branches of the NECC is calculated. Comparison of G12V1 circulation with the ADCP data shows the reliability of the G12V1 transport estimates in the first 150-m-depth (Figure 12a), in agreement with Verdy and Jochum (2005) and Urbano et al. (2006). The first 150-m-depth transport seasonal cycle (Figure 16) shows the maximum contribution of the sNECC around October-November (16 Sv), while the nNECC reaches its maximum in August-September (10 Sv), occurring when the ITCZ reaches its northernmost position. Then the nNECC transport decreases until vanishing in December. From December to May, the sNECC transport, contributing the full NECC system with the absence of the nNECC branch, decreases to quasi-vanish in May. Moreover, we found a direct relationship between the transport and its core velocity, respectively 22.7 and 15.4 Sv per m/s for the sNECC and nNECC. These sNECC and nNECC seasonal evolutions corroborate the NECC decay and vanishing already proposed by Hormann et al. (2012). In other terms, the nNECC generation, growth, northward migration from July to December can characterize the influence of the ITCZ position migrating southward from its northernmost boreal summer position. While the sNECC transport from January to May can characterize the influence of the wind stress curl second zero crossing.

The NECC system interannual variability at 38°W from 2 to 12°N shows year to year variations associated with propagations of positives and negatives anomalies throughout the year. Transport seasonal anomalies can represent 75% of the mean transport. Figure 17 shows NECC positive anomalies propagations, corresponding first to the detachment of the nNECC to the sNECC, then its northward migration. And second to the continuous evolution of the sNECC branch from June to May the next year (in particular in 1998-1999, 2001-2002, 2004-2005, 2017-2018). South of 6°N positive (1997, 1999, 2002, 2012, 2016) and negative (1993, 1995, 1998, 2002, 2006, 2007, 2008, 2009, 2011, 2014, 2015 and 2017) anomalies propagating southward witness anomalous displacement of the sNECC core position relative to the start of the new sNECC seasonal cycle from June to December. Hence anomalies of the intensity, position, northward propagation of the sNECC and nNECC branches can be related to NECC's transport anomalies (Figures 17b and 18). The negative anomalies of the transport in 1993-1994, 1995, 2002-2003, 2006-to-2009 and 2011 (Figure 18) occur with years when velocity positive anomalies exhibit propagation beyond 6°N and further north. While positive anomalies (1996-1997, 1999, 2004, 2012, 2016 in Figure 18) correspond to anomaly propagations mostly restrained south of 6°N. Which indicates that sNECC strong intensity south of 6°N lead to positive anomalies of the NECC's transport. Figure 17 shows during 1998-1999, 2001-2002, 2004-2005, and 2017-2018 connections between the sNECC the second semester and the following year, with continuity of positive anomalies starting south of 6°N to 7-9°N that are related to an increase of the NECC transport (Figure 18).

The G12V1 NECC system analysis allows to describe over years its two branches, sNECC and nNECC, characteristics in term of 0-150 m-depth transport, and core velocity, depth and position. Then for the first time, to infer the relationship with Tropical Atlantic variability through the AMM, AZM, ITCZ and WS6 indices (Figures 18 and 19). As mentioned by Chang et al. (2006), NECC's transport filtered time series show remarkable interannual positive and negative anomalies associated with warm and cold AMM and/or AZM phases, in particular in 1993-1994, 1997, 1999, 2002, 2004, 2006, 2009, 2011, 2012, 2014, 2016, when using a "above half-standard-deviation" threshold criteria. Three clear scenarii were found from filtered time series. First a NECC transport positive anomaly associated with positive AMM, negative AZM indices, ITCZ northward shift and positive wind stress anomaly at 6°N. Second a NECC transport positive anomaly associated with a AMM negative index, a positive AZM index, and no particular ITCZ and WS6 indices pattern. Third a NECC transport negative anomaly associated to negative AMM index, or a local minimum of AMM, a negative AZM index or a local minimum of AZM, a southward shift of the ITCZ and a wind stress negative anomaly at 6°N (but in 2015 with ITCZ and WS6 positive, but decreasing). Finally, a fourth scenario is observed, less clearly, for NECC transport negative anomalies, associated with positive AMM index, positive or decreasing AZM index, ITCZ southward shift and no clear wind stress pattern.

Hormann et al. (2012) using a complex empirical orthogonal function analyses stated that the NECC's transport strength was associated with the AZM while its latitudinal shift related to the AMM. Our analyses of sNECC and nNECC variability (Figure 19) show more complex relationship. Due to the strength and duration of the sNECC compared to the nNECC branch, positive/negative NECC and sNECC transports are linked. During the first period of the year, the AMM and sNECC transport anomaly correlation indicates that during "warm" AMM phase, the sNECC is strengthened. However, during positive anomaly NECC transport years, the sNECC transport anomaly can be weak or negative in March, with a positive AZM index. This is consistent with our finding of anticorrelated pattern of AZM phases with sNECC transport at the end of its cycle (December to April). During these years, the nNECC transport is stronger in November, with a positive AMM index that season. This is consistent with our evidence that the nNECC transport and position from October to December are significatively correlated with

AMM, ITCZ and WS6 indices. In other word, during AMM "warm" phase onsets, with ITCZ positions north-than-normal and a stronger wind stress at 6°N, the nNECC is intensified and occupies a position more north-than-normal, and the contrary occurs during AMM cold phases. Interestingly a positive correlation is found between the nNECC position in October-November and the sNECC core velocity in December-January. That is, the nNECC northward shift caused by AMM warm phase would witness an intensified sNECC branch, and conversely. This pattern corresponds to our second scenario, that occurs in 1996, 1999 and 2016.

We then found that the sNECC transport onset (June-July) is anticorrelated with the AZM index in February-May. According to Cabos et al. (2019) the AZM so-called "Atlantic Niño" is observed frequently in June driven by air-sea interactions, with direct impact on West African Monsoon precipitations, while the AMM, driven by the so-called wind-evaporation-SST mechanism, acts during the boreal spring (April to May) by influencing the precipitations over the tropical Atlantic and the North-East Brazil. Hence, an onset phase of Atlantic Niña event will be associated with a stronger sNECC branch from December to July. Anticorrelation between the sNECC position and the AMM and ITCZ indices are also noticed from August to December (during the first part of the sNECC cycle), and in January-February (when the sNECC starts its northward shift). This is what we observe with our first scenario in 1997, 2001, 2004 and 2012. Another situation appears during AMM cold phases, with an ITCZ located more south-than-normal and associated with a southward position of the sNECC, and when we can notice negative sNECC transport anomalies. The latter can be associated to the correlation with AMM cold phase, or the anticorrelation with positive AZM during the first part of the year. Negative or close to zero AZM index correspond to reduced sNECC negative transport anomalies. But the AMM cold phase is also associated with negative nNECC transport that can increase the negative effect on the total NECC value during that years. This occurs in 1994, 2002, 2009, 2014, 2015, and corresponds to our third scenario. At the opposite, in 1995 and 2011 (also negative NECC transport anomalous years), there is a positive AMM index that leads to close to zero nNECC anomalies. At the same time, the AZM positive phase is associated to stronger negative sNECC transport anomalies, which brings the fourth scenario we observed.

7 Conclusion

The PIRATA array annual servicing cruises provide from 2001 to 2018 fifteen ADCP surveys along the 38°W transect where are located four of the moorings. This allows to revisit the ADCP analyses proposed by Urbano et al. (2008) that used 8 surveys. The GLORYS12V1 global ocean reanalysis monthly averages or daily estimates with a 1/12° horizontal resolution offer an opportunity to study the three-dimensional circulation in the West Tropical Atlantic basin. The ADCP section's velocity profiles, not assimilated in G12V1, show that G12V1 offers a good estimation of observed currents along 38°W. In parallel, compared to the NOAA drifter-derived surface velocity monthly climatology, the overall circulation in the region from G12V1 represent a realistic annual and seasonal pattern of the currents yet described in the literature (e.g., Hormann et al., 2012).

From 2001 to 2018, the 15 years ADCP data from PIRATA-Brazil annual servicing cruises and CAMADAS FINAS experiment along 38°W transect are collected and processed to provide velocity profiles from 2°N to 15°N that intersect the main currents in the region. These synoptic profiles at different moment of the year allow to revisit the evolving pattern of the EUC, NEUC, nSEC, NECC and NEC branches proposed by Urbano et al. (2008) using eight surveys. To further analyze the regional patterns of these currents, the GLORYS12V1 (G12V1) global ocean eddy-permitting reanalysis provided by the CMEMS over the 1993-2018 period is used, together with the C3S ERA5 wind estimates, the NOAA OI SST v2 product, a CMEMS SSS product and the NOAA/AOML surface velocity climatology from drifters. The latter provides the annual and seasonal pattern of the currents yet described in the literature (e.g., Hormann et al., 2012). Evaluated against it, G12V1 witnesses a realistic representation of the circulation seasonal variability in the region. The comparison of G12V1 vertical velocity sections with ADCP transects offers a synoptic and quantitative evaluation of the model estimates. In particular because neither the ADCP nor the drifter data are assimilated into the G12V1 reanalysis. The 0-150-m depth transport estimated from G12V1, in particular from the NECC, are matching ADCP measured values with good agreement and gives good confidence on the reliability of further analysis of G12V1 vertical currents along 38°W.

This study at 38°W from 2°N to 15°N allows to focus on the NECC variability, and confirms the seasonal varying two-branch pattern proposed by Urbano et al. (2008). The NECC characteristics are revisited: the presence of the two cores/branches of the NECC; its volume transports; and the core's velocity, depth, and positions are updated. The G12V1 monthly estimates allow to improve the sNECC and nNECC seasonal cycle pattern forced by the wind stress curl. Starting in June, the NECC seasonal cycle is initiated with a sNECC branch that grows, extend northward, detaching a nNECC core migrating to the north that vanishes in December. This first part of the cycle is driven by the ITCZ and associated wind curl pattern. Then from January to May, the sNECC migrate northward and decays, under the influence of the wind stress curl second zero crossing lying north of 10°N. In conjunction with the ITCZ, the total volume transport of NECC follows an annual cycle that is impacted by the Rossby waves coming from African coast from June to November that deepen the thermocline and then the sNECC core. The transport seasonal pattern varies on average from 1 Sv in May when the sNECC is the weakest, to 24 Sv in October (more than 32 Sv estimated by G12V1 in 2012). Note that sNECC core intensity is stronger (0.7 m/s) in November. The sNECC and the nNECC extends resp. between 3-10°N with an average position at 6°N±1.2° and between 6.5-12°N with an average position at 8.3°N±0.8°. Their average depths are resp. 47±6m and 39±5.3m.

Over 1993 to 2018, the G12V1 reanalysis allows to revisit the relationship between the NECC and the Atlantic climatic modes initiated by Hormann et al. (2012), by characterizing the interannual variations of the sNECC and nNECC branches. For the first time, their transport, core velocity strength, position and depth are analyzed with regard to Atlantic Meridional (AMM) and Zonal (AZM) Mode evolutions. First, relations between these modes, ITCZ position and wind stress curl interannual anomalies at 38°N yet described in the literature are confirmed. The AMM warm/cold phase induce anomalous northward/southward ITCZ position, and negative AZM so-called "Atlantic Niña" also strengthen positive shift of the ITCZ. Then, G12V1 allow to draw a more detailed image of the interannual variations of the NECC characteristics in relation with these four indices. The sNECC branch, more important than the nNECC branch and evolving all along the year, is the major contributor to the NECC's system variability. We found direct relation between the sNECC transport interannual anomalies and the AMM, ITCZ and wind stress anomalies during the year, and anticorrelation with AZM during the first part of the year. Moreover the nNECC transport and position interannual anomalies from September to December are correlated with the AMM phases. Three clear scenarii are proposed over these years. First, positive AMM and negative AZM phases bring to positive NECC transport. A second positive transport NECC scenario appears during positive AZM phase, with weaker but negative AMM phase. Then, the most relevant scenario for NECC transport negative anomalies is associated to AMM negative phases, with AZM index negative or positive but decreasing, phase. And associated with a southward shift of the ITCZ and a wind stress negative anomaly at 6°N.

This work and the characterization of the NECC branches variability opens the door for further investigations on their contribution to the overall tropical Atlantic circulation, both at the western boundary and over the entire basin. In particular in the eastward advection of salt anomalies. It gives also credit to G12V1 to be used for further studies in the whole tropical Atlantic basin. At the interannual time scale the study highlighted many aspects of the relationship between the NECC, the wind stress curl and the two climatic modes of the Atlantic and can be taken as precursor for further investigations of the role of the interannual variability of the currents on the predictability of the rainfall fluctuations over the west tropical Atlantic regions (Cabos et al., 2019; Chang et al., 2006; Hormann et al., 2012). This work shows finally that ocean observing programs like PIRATA are key in the tropical Atlantic, in order to maintain our capability to characterize precisely the ocean circulation, validate further on numerical modelling, and ingest observations into assimilated simulation to increase realism.

Author contribution

Djoirka M. Dimoune performed the ADCP and GLORYS2V1 analyses as part of his PhD thesis research, Fabrice Hernandez contributed to these tasks and performed complementary analyses. Fabrice Hernandez and Moacyr Araujo provided an overall supervision of this study.

Acknowledgements

We are grateful to PIRATA Brazil for providing the ADCP data. Pre-processed Camadas Finas ADCP data were provided by Pr. Alex Costa. We particularly thank Gerard Eldin for his advices in processing the ADCP data, Jean-Michel Lellouche, Marie Drévillon and Charly Régnier from Mercator Océan International for exchanges on the GLORYS12V1 reanalysis. ADCP data and reanalysis results are available at https://sites.ufpe.br/ceerma/ (CEERMA/UFPE) and https://marine.copernicus.eu/ (CMEMS/EU), respectively. We are also grateful to the CMEMS, the ECMWF and the NOAA respectively who made available the ocean reanalysis, the mean wind fields and SST products, and drifter-derived climatology near surface data for this work. We are also thankful to CAPES Foundation. Fabrice Hernandez supervised this work as part of the TAPIOCA Laboratoire Mixte International funded by IRD and CAPES/MEC in Brazil. Moacyr Araujo thanks the support of the Brazilian Research Network on Global Climate Change FINEP/Rede CLIMA (grants 01.13.0353-00). This work has been supported by the French LEFE/GMMC funded project Merca2Recife (42-DS-GMMC-MERCA2RECIFE – REF. CNRS N° 197932), and also represents a contribution to the INCT AmbTropic, the Brazilian National Institute of Science and Technology for Tropical Marine Environments, CNPq/FAPESB (grants 565054/2010-4 and 8936/2011 and 465634/2014-1), and to the TRIATLAS project, which has received funding from the European Union's Horizon 2020 research and innovation program under grant agreement No 817578.

References

Aguedjou, H. M. A., I. Dadou, A. Chaigneau, Y. Morel, and G. Alory, (2019). Eddies in the Tropical Atlantic Ocean and Their Seasonal Variability. Geophys Res Lett, 46 (21), 12156-12164. doi: 10.1029/2019gl083925.

Bourlès, B., Y. Gouriou, and R. Chuchla, (1999). On the circulation in the upper layer of the western equatorial Atlantic. Journal of Geophysical Research: Oceans, 104 (C9), 21151-21170. doi: 10.1029/1999jc900058.

Bourlès, B., and Coauthors, (2008). The PIRATA program: History, Acomplishments, and Future Directions. Bul. Amer. Met. Soc., 89 (8), 1111-1125. doi: DOI:10.1175/2008BAMS2462.1.

Bourlès, B., and Coauthors, (2019). PIRATA: A Sustained Observing System for Tropical Atlantic Climate Research and Forecasting. Earth and Space Science. doi: 10.1029/2018EA000428.

Cabanes, C., and Coauthors, (2013). The CORA dataset: validation and diagnostics of in-situ ocean temperature and salinity measurements. Ocean Sci., 9 (1), 1-18. doi: 10.5194/os-9-1-2013.

Cabos, W., A. de la Vara, and S. Koseki, (2019). Tropical Atlantic Variability: Observations and Modeling. Atmosphere, 10 (9), 502.

Carton, J. A., and E. J. Katz, (1990). Estimates of the zonal slope and seasonal transport of the Atlantic North Equatorial Countercurrent. Journal of Geophysical Research: Oceans, 95 (C3), 3091-3100. doi: 10.1029/JC095iC03p03091.

Carton, J. A., X. Cao, B. S. Giese, and A. M. D. Silva, (1996). Decadal and Interannual SST Variability in the Tropical Atlantic Ocean. J. Phys. Oceanogr., 26 (7), 1165-1175. doi: 10.1175/1520-0485(1996)026<1165:Daisvi>2.0.Co;2.

Castelão, G. P., and W. E. Johns, (2011). Sea surface structure of North Brazil Current rings derived from shipboard and moored acoustic Doppler current profiler observations. Journal of Geophysical Research: Oceans, 116 (C1). doi: 10.1029/2010jc006575.

Castellanos, P., J. L. Pelegrí, E. J. D. Campos, M. Rosell-Fieschi, and M. Gasser, (2015). Response of the surface tropical Atlantic Ocean to wind forcing. Progr. in Oceanogr., 134271-292. doi: 10.1016/j.pocean.2015.02.005.

Chang, P., and Coauthors, (2006). Climate Fluctuations of Tropical Coupled Systems—The Role of Ocean Dynamics. J. Climate, 19 (20), 5122-5174. doi: 10.1175/jcli3903.1.

Chepurin, G., and J. A. Carton, (1997). The hydrography and circulation of the upper 1200 meters in the tropical North Atlantic during 1982-91. J. Mar. Res., 55 (4), 633-670. doi: 10.1357/0022240973224238.

Cleveland, W. S., and S. J. Devlin, (1988). Locally Weighted Regression: An Approach to Regression Analysis by Local Fitting. Journal of the American Statistical Association, 83 (403), 596-610. doi: 10.1080/01621459.1988.10478639.

Coles, V. J., M. T. Brooks, J. Hopkins, M. R. Stukel, P. L. Yager, and R. R. Hood, (2013). The pathways and properties of the Amazon River Plume in the tropical North Atlantic

Ocean. Journal of Geophysical Research: Oceans, 118 (12), 6894-6913. doi: 10.1002/2013jc008981.

Didden, N., and F. Schott, (1992). Seasonal variations in the western tropical Atlantic: Surface circulation from Geosat altimetry and WOCE model results. Journal of Geophysical Research: Oceans, 97 (C3), 3529-3541. doi: 10.1029/91jc02860.

Drévillon, M., C. Régnier, J.-M. Lellouche, G. Garric, C. Bricaud, and O. Hernandez, 2018: QUALITY INFORMATION DOCUMENT For Global Ocean Reanalysis Products GLOBAL-REANALYSIS-PHY-001-030 v1.2. (CMEMS-GLO-QUID-001-030), ed. by Mercator Ocean International, pub. by C. M. E. M. Service, 48 pp pp. [Available at http://marine.copernicus.eu/documents/QUID/CMEMS-GLO-QUID-001-030.pdf.]

Enfield, D. B., A. M. Mestas-Nuñez, D. A. Mayer, and L. Cid-Serrano, (1999). How ubiquitous is the dipole relationship in tropical Atlantic sea surface temperatures? Journal of Geophysical Research: Oceans, 104 (C4), 7841-7848. doi: 10.1029/1998jc900109.

Foltz, G. R., M. J. McPhaden, and R. Lumpkin, (2012). A Strong Atlantic Meridional Mode Event in 2009: The Role of Mixed Layer Dynamics. J. Climate, 25 (1), 363-380. doi: 10.1175/JCLI-D-11-00150.1.

Fonseca, C. A., G. J. Goni, W. E. Johns, and E. J. D. Campos, (2004). Investigation of the North Brazil Current retroflection and North Equatorial Countercurrent variability. Geophys Res Lett, 31 (21). doi: 10.1029/2004gl020054.

Gaillard, F., T. Reynaud, V. Thierry, N. Kolodziejczyk, and K. von Schuckmann, (2016). In Situ–Based Reanalysis of the Global Ocean Temperature and Salinity with ISAS: Variability of the Heat Content and Steric Height. J. Climate, 29 (4), 1305-1323. doi: 10.1175/jcli-d-15-0028.1.

Garzoli, S., and P. L. Richardson, (1989). Low-frequency meandering of the Atlantic North Equatorial Countercurrent. Journal of Geophysical Research: Oceans, 94 (C2), 2079-2090. doi: 10.1029/JC094iC02p02079.

Garzoli, S. L., (1992). The Atlantic North Equatorial Countercurrent: Models and observations. Journal of Geophysical Research: Oceans, 97 (C11), 17931-17946. doi: 10.1029/92jc01363.

Garzoli, S. L., and E. J. Katz, (1983). The Forced Annual Reversal of the Atlantic North Equatorial Countercurrent. J. Phys. Oceanogr., 13 (11), 2082-2090. doi: 10.1175/1520-0485(1983)013<2082:Tfarot>2.0.Co;2.

Garzoli, S. L., A. Ffield, W. E. Johns, and Q. Yao, (2004). North Brazil Current retroflection and transports. Journal of Geophysical Research: Oceans, 109 (C1). doi: 10.1029/2003jc001775.

Goni, G. J., and W. E. Johns, (2001). A census of North Brazil Current Rings observed from TOPEX/POSEIDON altimetry: 1992–1998. Geophys Res Lett, 28 (1), 1-4. doi: 10.1029/2000gl011717.

Good, S. A., M. J. Martin, and N. A. Rayner, (2013). EN4: Quality controlled ocean temperature and salinity profiles and monthly objective analyses with uncertainty estimates. Journal of Geophysical Research: Oceans, 118 (12), 6704-6716. doi: 10.1002/2013jc009067.

Hormann, V., and P. Brandt, (2007). Atlantic Equatorial Undercurrent and associated cold tongue variability. J. Geophys. Res.-Oceans, 112 (C6). doi: 10.1029/2006jc003931.

Hormann, V., R. Lumpkin, and G. R. Foltz, (2012). Interannual North Equatorial Countercurrent variability and its relation to tropical Atlantic climate modes. Journal of Geophysical Research: Oceans, 117 (C4). doi: 10.1029/2011jc007697.

Katz, E. J., (1981). Dynamic topography of the sea surface in the equatorial Atlantic. J. Mar. Res., 3953-63.

Kermabon, C., P. Lherminier, P. Le bot, and F. Gaillard, 2018: Chaine Automatisée de Suivi des Courantomètres Acoustiques Doppler Embarqués. CASCADE V7.2: Logiciel de validation et de visualisation des mesures ADCP de coque. Documentation utilisateur et maintenance. (ODE/LOPS 18), ed. by Ifremer, Brest, France, 115 pp. [Available at ftp://ftp.ifremer.fr/ifremer/lpo_permanents/cascade/CASCADE_V72_V2.pdf.]

Laurindo, L. C., A. J. Mariano, and R. Lumpkin, (2017). An improved near-surface velocity climatology for the global ocean from drifter observations. Deep-Sea Res Pt I, 12473-92. doi: 10.1016/j.dsr.2017.04.009.

Lellouche, J.-M., and Coauthors, (2018). Recent updates to the Copernicus Marine Service global ocean monitoring and forecasting real-time 1⁄12° high-resolution system. Ocean Sci., 14 (5), 1093-1126. doi: 10.5194/os-14-1093-2018.

Lumpkin, R., and S. L. Garzoli, (2005). Near-surface circulation in the Tropical Atlantic Ocean. Deep-Sea Res Pt I, 52 (3), 495-518. doi: 10.1016/j.dsr.2004.09.001.

Madec, G., 2008: NEMO ocean engine - Version 3.1. Note du Pôle de modélisation, (27), ed. by Institut Pierre-Simon Laplace (IPSL), Paris, France1288-1619, 201 pp

Philander, S. G. H., and R. C. Pacanowski, (1986). The mass and heat budget in a model of the tropical Atlantic Ocean. Journal of Geophysical Research: Oceans, 91 (C12), 14212-14220. doi: 10.1029/JC091iC12p14212.

Reynolds, R. W., N. A. Rayner, T. M. Smith, D. C. Stokes, and W. Wang, (2002). An Improved In Situ and Satellite SST Analysis for Climate. J. Climate, 15 (13), 1609-1625. doi: 10.1175/1520-0442(2002)015<1609:Aiisas>2.0.Co;2.

Richardson, P. L., and T. K. McKee, (1984). Average Seasonal Variation of the Atlantic Equatorial Currents from Historical Ship Drifts. J. Phys. Oceanogr., 14 (7), 1226-1238. doi: 10.1175/1520-0485(1984)014<1226:Asvota>2.0.Co;2.

Richardson, P. L., and D. Walsh, (1986). Mapping climatological seasonal variations of surface currents in the tropical Atlantic using ship drifts. Journal of Geophysical Research: Oceans, 91 (C9), 10537-10550. doi: 10.1029/JC091iC09p10537.

Richardson, P. L., and G. Reverdin, (1987). Seasonal cycle of velocity in the Atlantic North Equatorial Countercurrent as measured by surface drifters, current meters, and ship drifts. Journal of Geophysical Research: Oceans, 92 (C4), 3691-3708. doi: 10.1029/JC092iC04p03691.

Rio, M.-H., and F. Hernandez, (2003). High frequency response of wind-driven currents measured by drifting buoys and altimetry over the world ocean. J Geophys Res, 108 (C8), 39-31. doi: 10.1029/2002JC001655.

Rosell-Fieschi, M., J. L. Pelegrí, and J. Gourrion, (2015). Zonal jets in the equatorial Atlantic Ocean. Progr. in Oceanogr., 130 (0), 1-18. doi: 10.1016/j.pocean.2014.08.008.

Schott, F. A., and C. W. Böning, (1991). The WOCE model in the western equatorial Atlantic: Upper layer circulation. Journal of Geophysical Research: Oceans, 96 (C4), 6993-7004. doi: 10.1029/90jc02683.

Schott, F. A., J. Fischer, and L. Stramma, (1998). Transports and pathways of the upper-layer circulation in the western tropical Atlantic. J. Phys. Oceanogr., 28 (10), 1904-1928. doi: 10.1175/1520-0485(1998)028<1904:tapotu>2.0.co;2.

Schouten, M. W., R. P. Matano, and T. P. Strub, (2005). A description of the seasonal cycle of the equatorial Atlantic from altimeter data. Deep-Sea Res Pt I, 52 (3), 477-493. doi: 10.1016/j.dsr.2004.10.007.

Servain, J., (1991). Simple climatic indices for the tropical Atlantic Ocean and some applications. Journal of Geophysical Research: Oceans, 96 (C8), 15137-15146. doi: 10.1029/91jc01046.

Stramma, L., (1991). Geostrophic transport of the South Equatorial Current in the Atlantic. J. Mar. Res., 49 (2), 281-294. doi: 10.1357/002224091784995864.

Stramma, L., and F. A. Schott, (1999). The mean flow field of the tropical Atlantic Ocean. Deep-Sea Res Pt II, 46 (1-2), 279-303. doi: 10.1016/s0967-0645(98)00109-x.

The DRAKKAR Group, and Coauthors, (2014). DRAKKAR: developing high resolution ocean components for European Earth system models. CLIVAR Exchanges, 19 (2), 18-21.

Urbano, D. F., M. Jochum, and I. C. A. da Silveira, (2006). Rediscovering the second core of the Atlantic NECC. Ocean Model., 12 (1), 1-15. doi: 10.1016/j.ocemod.2005.04.003.

Urbano, D. F., R. A. F. De Almeida, and P. Nobre, (2008). Equatorial Undercurrent and North Equatorial Countercurrent at 38°W: A new perspective from direct velocity data. Journal of Geophysical Research: Oceans, 113 (C4). doi: 10.1029/2007jc004215.

Varona, H. L., D. Veleda, M. Silva, M. Cintra, and M. Araujo, (2019). Amazon River plume influence on Western Tropical Atlantic dynamic variability. Dynam. Atmos. Oceans, 851-15. doi: 10.1016/j.dynatmoce.2018.10.002.

Verdy, A., and M. Jochum, (2005). A note on the validity of the Sverdrup balance in the Atlantic North Equatorial Countercurrent. Deep-Sea Res Pt I, 52 (1), 179-188. doi: 10.1016/j.dsr.2004.05.014.

Vialar, J., 1978: Calcul des probabilités et statistiques. Statistiques, contingences et corrélations., ed. by Secrétariat général de l'Aviation Civile, Direction de la Météorologie.Cours du Ministère des Transports, Tome 3

Wilson, W. D., W. E. Johns, and S. L. Garzoli, (2002). Velocity structure of North Brazil Current rings. Geophys Res Lett, 29 (8), 114-111-114-114. doi: 10.1029/2001gl013869.

Zebiak, S. E., (1993). Air–Sea Interaction in the Equatorial Atlantic Region. J. Climate, 6 (8), 1567-1586. doi: 10.1175/1520-0442(1993)006<1567:Aiitea>2.0.Co;2.

Figure 1.

NEC
NBCR
NECC
Guyana C.
Guinea C.
nSEC
NBC
SEC
cSEC
sSEC
0.5 m.s-1
18°N
12°N
6°N
0°
6°S
12°S
18°S
60°W
50°W
40°W
30°W
20°W
10°W
0°
10°E
SSS standard deviation (psu)
0.30
0.35
0.40
0.50
1.50
3.00

Figure 2.

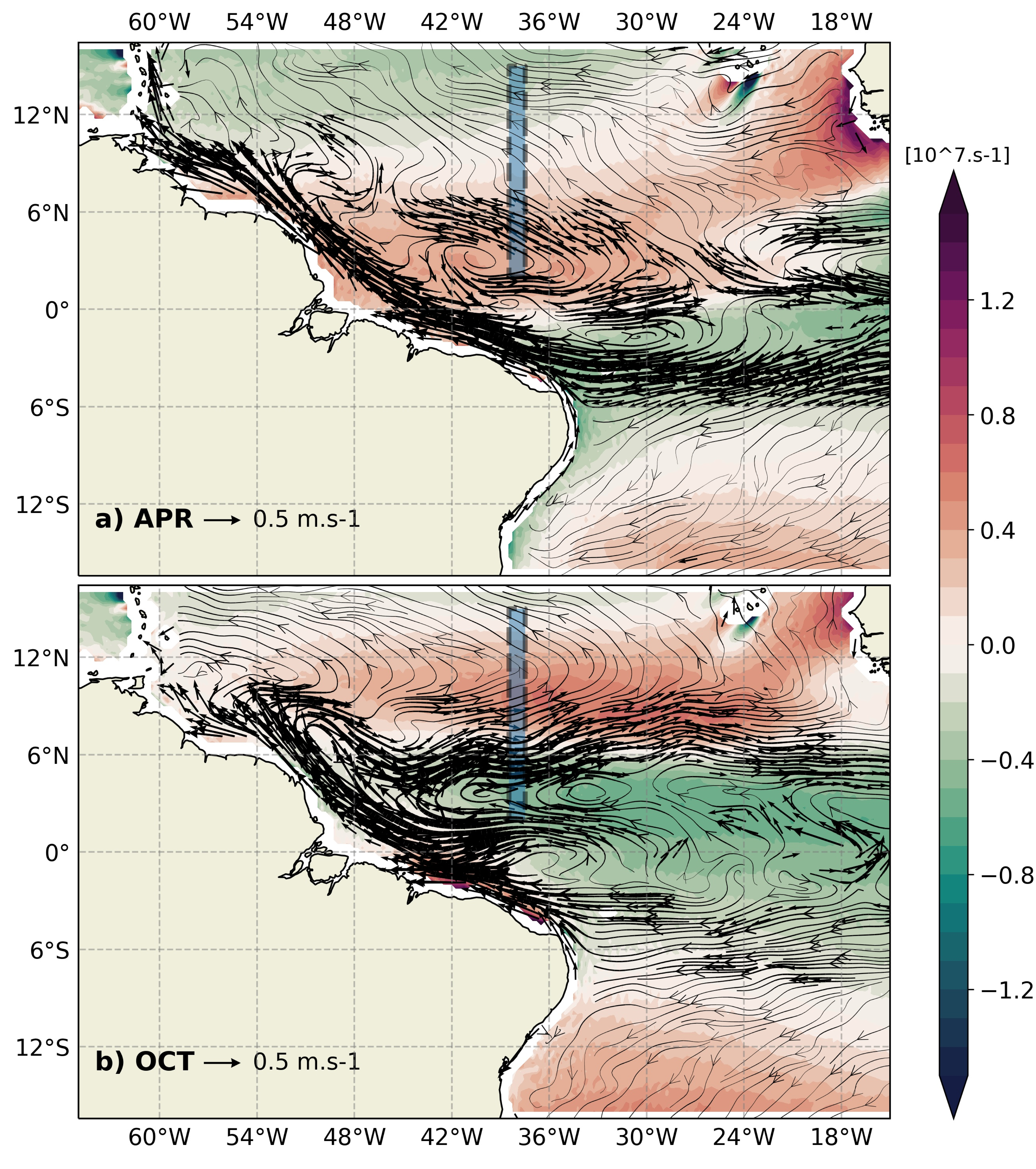

60°W
54°W
48°W
42°W
36°W
30°W
24°W
18°W
12°N
6°N
0°
6°S
12°S
a) APR
0.5 m.s-1
b) OCT
0.5 m.s-1
[10^7.s-1]
1.2
0.8
0.4
0.0
−0.4
−0.8
−1.2

Figure 3.

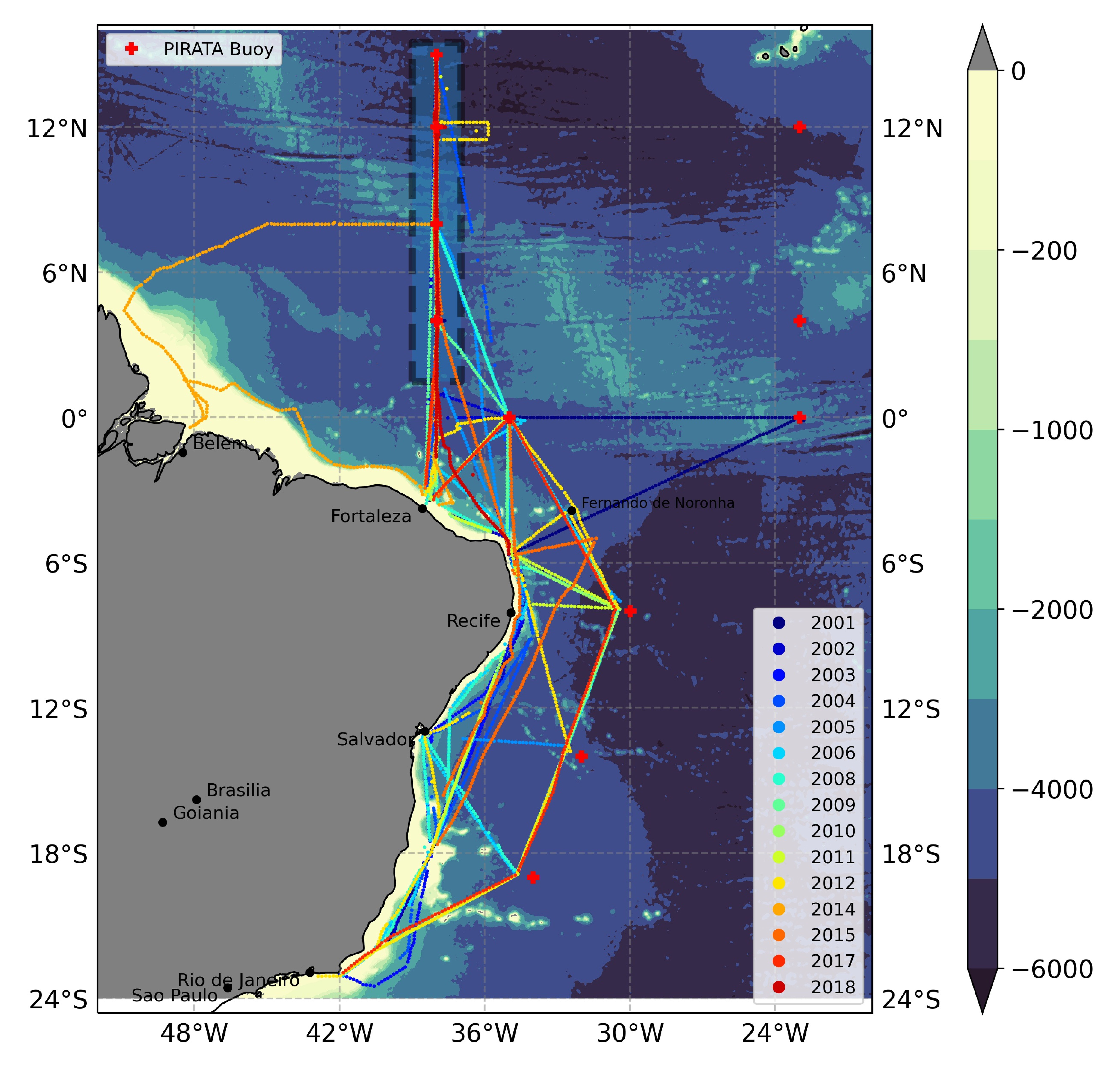
PIRATA Buoy
12°N
6°N
0°
6°S
12°S
18°S
24°S
48°W
42°W
36°W
30°W
24°W
Belem
Fortaleza
Fernando de Noronha
Recife
Salvador
Brasilia
Goiania
Rio de Janeiro
Sao Paulo
2001
2002
2003
2004
2005
2006
2008
2009
2010
2011
2012
2014
2015
2017
2018
0
−200
−1000
−2000
−4000
−6000

Figure 4.


a) 21-31/03/2009
b) 05-12/04/2002
c) 02-08/04/2008
d) 09-15/04/2001
nSEC
sNECC
NEUC
nNECC
EUC
0
-50
-100
-150
-200
-250
2°N
4°N
6°N
8°N
10°N
12°N
14°N

Figure 5.


a) 19-26/10/2018
b) 14-22/11/2017
c) 27/10-/03/11/2015
d) 27-31/10/2012
e) 29/08-13/09/2011
f) 01-07/12/2006
g) 03-28/07/2014
h) 24-30/07/2010
i) 14-19/07/2011
j) 21-27/07/2005
k) 17-31/07/2003
nSEC
sNECC
nNECC
NEUC
0
-50
-100
-150
-200
-250
2°N
4°N
6°N
8°N
10°N
12°N
14°N

Figure 6.

a)
Transport (Sv)
0
10
20
30
Ap/01
Ap/02
Jl/03
Jl/04
Jl/05
Dc/06
Ap/08
Mr/09
Jl/10
At/11
Oc/12
Jl/14
Nv/15
Nv/17
Oc/18
Time
30-100m
30-150m
30-200m
b)
Transport (Sv)
0
10
20
Mar/Apr
Jul
Oct/Nov/Dec
Month

Figure 7.


a)
b)
c)
Belem
Fortaleza
Recife
Salvador
12°N
6°N
0°
6°S
12°S
63°W
54°W
45°W
36°W
27°W
1.5
1.4
1.3
1.2
1.1
1
0.9
0.8
0.7
0.6
0.5
60
50
40
30
20
10
0
-10
-20
-30
-40
-50
-60
Ratio Drifters - G12V1
Angle Drifters - G12V1
Latitude
2.125°N
3.125°N
4.125°N
5.125°N
6.125°N
7.125°N
8.125°N
9.125°N
10.125°N
11.125°N
12.125°N
13.125°N
14.125°N

Figure 8.

a)
b)
c)
d)
Belem
Fortaleza
Recife
Salvador
12°N
6°N
0°
6°S
12°S
63°W
54°W
45°W
36°W
27°W
Correlations
RMSDiff.
Latitude
Norm
Angle
2.125°N
3.125°N
4.125°N
5.125°N
6.125°N
7.125°N
8.125°N
9.125°N
10.125°N
11.125°N
12.125°N
13.125°N
14.125°N

Figure 9.

Drifters
G12V1
0.3 m/s
15°N
14°N
13°N
12°N
11°N
10°N
9°N
8°N
7°N
6°N
5°N
4°N
3°N
2°N
Latitudes
Jan
Feb
Mar
Apr
May
Jun
Jul
Aug
Sep
Oct
Nov
Dec
Months

Figure 10.

Stretch
Rotation
Vector correlation
Coefficient
1
0.9
0.8
0.7
0.6
0.5
0.4
0.3
0.2
0.1
0
-0.1
-0.2
-0.3
-0.4
-0.5
-0.6
Ap/01
Ap/02
Jl/03
At/04
Jl/05
Dc/06
Ap/08
Mr/09
Jl/10
At/11
Oct/12
Jl/14
Nv/15
Nv/17
Oct/18
Time

Figure 11.

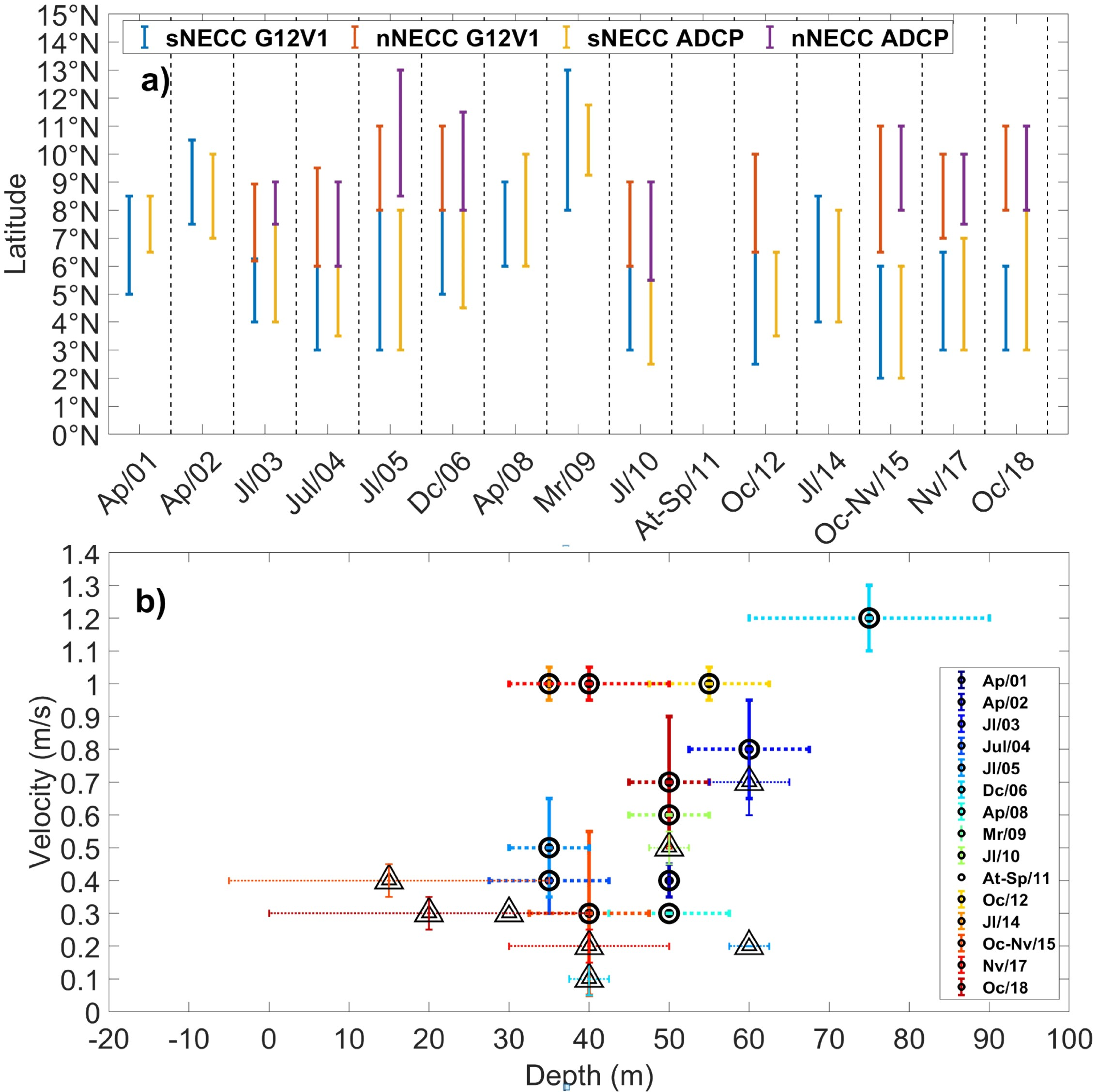

a)
sNECC G12V1
nNECC G12V1
sNECC ADCP
nNECC ADCP
Latitude
0°N
1°N
2°N
3°N
4°N
5°N
6°N
7°N
8°N
9°N
10°N
11°N
12°N
13°N
14°N
15°N
Ap/01
Ap/02
Jl/03
Jul/04
Jl/05
Dc/06
Ap/08
Mr/09
Jl/10
At-Sp/11
Oc/12
Jl/14
Oc-Nv/15
Nv/17
Oc/18
b)
Velocity (m/s)
Depth (m)
0
0.1
0.2
0.3
0.4
0.5
0.6
0.7
0.8
0.9
1
1.1
1.2
1.3
1.4
-20
-10
0
10
20
30
40
50
60
70
80
90
100
Ap/01
Ap/02
Jl/03
Jul/04
Jl/05
Dc/06
Ap/08
Mr/09
Jl/10
At-Sp/11
Oc/12
Jl/14
Oc-Nv/15
Nv/17
Oc/18

Figure 12.

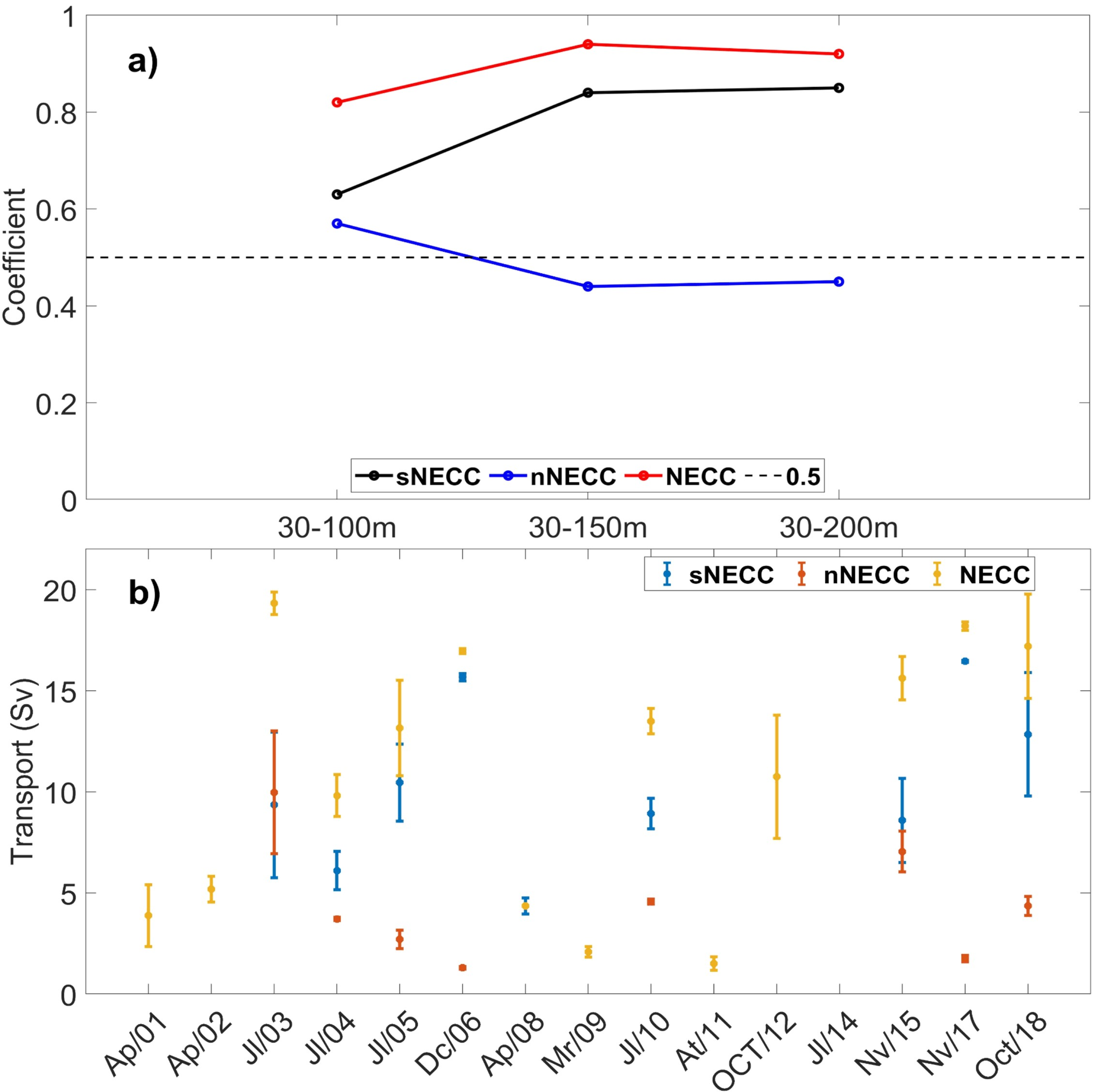

a)
Coefficient
sNECC
nNECC
NECC
0.5
30-100m
30-150m
30-200m
b)
Transport (Sv)
sNECC
nNECC
NECC
Ap/01
Ap/02
Jl/03
Jl/04
Jl/05
Dc/06
Ap/08
Mr/09
Jl/10
At/11
OCT/12
Jl/14
Nv/15
Nv/17
Oct/18

Figure 13.

Jan
Feb
Mar
Apr
May
Jun
Jul
Aug
Sep
Oct
Nov
Dec
nSEC
sNECC
nNECC
EUC
NEUC
0
-50
-100
-150
-200
-250
-300
-350
-400
2°N
4°N
6°N
8°N
10°N
12°N
14°N

Figure 14.


12°N
6°N
0°
6°S
12°S
a)
Belem
Fortaleza
Recife
Salvador
0.2 m/s
G12V1-50m: April
12°N
6°N
0°
6°S
12°S
b)
Belem
Fortaleza
Recife
Salvador
0.2 m/s
G12V1 0-45m: June
63°W
54°W
45°W
36°W
27°W

Figure 15.

ITCZ
2nd zero curl
15°N
14°N
13°N
12°N
11°N
10°N
9°N
8°N
7°N
6°N
5°N
4°N
3°N
2°N
0.05 N/m2
0.46 m/s
Jan
Feb
Mar
Ap
May
Jun
Jul
Aug
Sep
Oct
Nov
Dec

Figure 16.

sNECC
nNECC
NECC
ITCZ
2nd zero curl
Zonal transport
0
5
10
15
20
25
Zero wind stress curl position
5°S
4°S
3°S
2°S
1°S
EQ
1°N
2°N
3°N
4°N
5°N
6°N
7°N
8°N
9°N
10°N
11°N
12°N
13°N
14°N
Dec
Jan
Feb
Mar
Apr
May
Jun
Jul
Aug
Sep
Oct
Nov
Dec
Jan
Month

Figure 17.

11°N
9°N
7°N
5°N
3°N
1
0.5
0
-0.5
-1
0.6
0.4
0.2
-0.2
-0.4
1993
1994
1995
1996
1997
1998
1999
2000
2001
2002
2003
2004
2005
2006
2007
2008
2009
2010
2011
2012
2013
2014
2015
2016
2017
2018

Figure 18.


NECC transport anomaly [Sv]
Normalized indices
Time
4
3
2
1
0
−1
−2
−3
−4
2.0
1.5
1.0
0.5
0.0
−0.5
−1.0
−1.5
−2.0
1994
1995
1996
1997
1998
1999
2000
2001
2002
2003
2004
2005
2006
2007
2008
2009
2010
2011
2012
2013
2014
2015
2016
2017
2018
NECC transport anomaly
ITCZ
AMM
AZM
Merid. Wind Anom. 6°N

Figure 19.


a)
sNECC transport anomaly
sNECC core vel. anomaly
sNECC core depth anomaly
sNECC core latitude anomaly
Vel. anom. [m.s-1]
Lat. anom. [deg]
0.15
0.10
0.05
0.00
−0.05
−0.10
−0.15
1.0
0.5
0.0
−0.5
−1.0
b)
NECC transp. [Sv]
Normalized indices
4
2
0
−2
−4
1
−1
c)
nNECC core vel. anomaly
nNECC core depth anomaly
nNECC core latitude anomaly
Vel. anom. [m.s-1]
Depth anom. [m]
12
9
6
3
−3
−6
−9
−12
1994
1995
1996
1997
1998
1999
2000
2001
2002
2003
2004
2005
2006
2007
2008
2009
2010
2011
2012
2013
2014
2015
2016
2017
2018
Time